

DUNE as the Next-Generation Solar Neutrino Experiment

Francesco Capozzi,^{1,2,3} Shirley Weishi Li,^{1,2,4} Guanying Zhu,^{1,2} and John F. Beacom^{1,2,5}

¹Center for Cosmology and AstroParticle Physics (CCAPP), Ohio State University, Columbus, OH 43210

²Department of Physics, Ohio State University, Columbus, OH 43210

³Max-Planck-Institut für Physik (Werner-Heisenberg-Institut), 80805 München, Germany

⁴SLAC National Accelerator Laboratory, Menlo Park, CA, 94025

⁵Department of Astronomy, Ohio State University, Columbus, OH 43210

(Dated: 24 August, 2018)

We show that the Deep Underground Neutrino Experiment (DUNE) has the potential to deliver world-leading results in solar neutrinos. Significant but realistic new efforts would be required. With an exposure of 100 kton-year, DUNE could detect $\gtrsim 10^5$ signal events above 5 MeV. Separate precision measurements of neutrino-mixing parameters and the ^8B flux could be made using two detection channels ($\nu_e + {}^{40}\text{Ar}$ and $\nu_{e,\mu,\tau} + e^-$) and the day-night effect ($> 10\sigma$). New particle physics may be revealed through the comparison of solar neutrinos (with matter effects) and reactor neutrinos (without), which is discrepant by $\sim 2\sigma$ (and could become 5.6σ). New astrophysics may be revealed through the most precise measurement of the ^8B flux (to 2.5%) and the first detection of the *hep* flux (to 11%). *DUNE is required*: No other experiment, even proposed, has been shown capable of fully realizing these discovery opportunities.

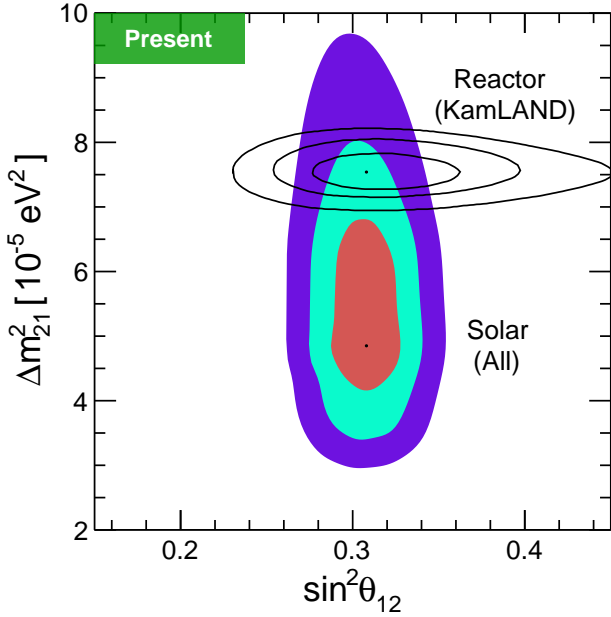


FIG. 1. Present measurements (1, 2, 3- σ) of neutrino mixing with solar [1–6] and reactor [7] neutrinos.

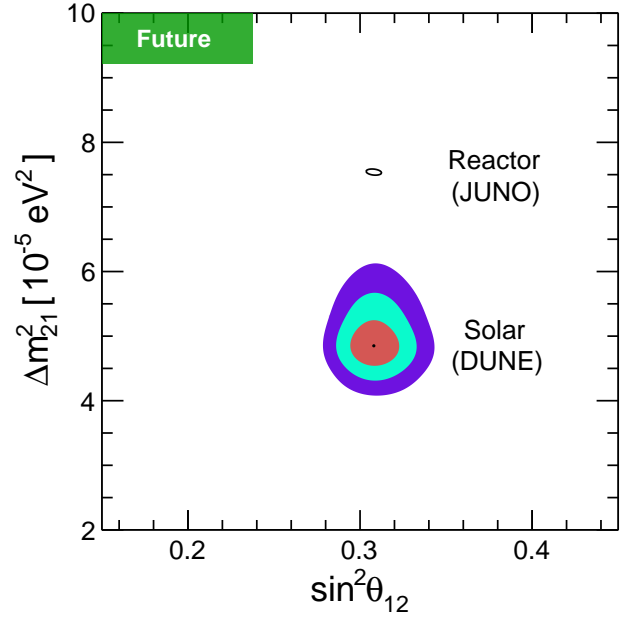


FIG. 2. Future precision of neutrino mixing with solar (DUNE alone; 1, 2, 3- σ) and reactor (JUNO alone; 3- σ [8, 9]) neutrinos, using present best-fit points and 100 kton-year for each.

Introduction.— Tremendous scientific opportunities remain in solar neutrinos. What are the particle properties of neutrinos? What are the nuclear processes that power our Sun and other stars? Although the basics are known [1–6], there are multiple unknowns and discrepancies. To progress, we need precise measurements of all neutrino-producing processes, plus ways to isolate new physics from new astrophysics. Here we focus on high energies (> 5 MeV).

For particle physics, the primary opportunity is to test for new physics through a precision comparison of neutrino-mixing parameters [10–16] measured in solar

versus reactor experiments. Figures 1 and 2 preview this. The contrast in physical conditions is striking: neutrinos versus antineutrinos, matter versus vacuum mixing, plus a much larger distance, the presence of magnetic fields, and more. There is a $\sim 2\text{-}\sigma$ discrepancy between the solar and reactor Δm^2_{21} values [6, 7, 17, 18]. The reactor measurement will soon be greatly improved by the JUNO experiment [8], but testing new physics — through both Δm^2_{21} and $\sin^2 \theta_{12}$ — depends on improving the solar measurement as well.

For astrophysics, the primary opportunity is to precisely measure the ^8B flux, which is extremely sensi-

tive to the solar core temperature ($\sim T_c^{25}$ [19]), and which is an important ingredient for resolving the solar-metallicity discrepancy [20–24]. Discovery of the *hep* flux, the highest-energy neutrino process, would probe physical conditions much further from the solar center than does the ^8B flux [21, 22].

How can these opportunities be realized, especially simultaneously? To go far beyond previous results requires a powerful new experiment at the multi-10-kton scale, plus breakthroughs in detection strategy.

We propose that DUNE — intended to make transformative studies of high-energy long-baseline neutrino mixing, proton decay, and supernova neutrino bursts [25–27] — has the potential to do the same for solar neutrinos. Building on prior work on solar-neutrino detection in liquid argon [28–31], our paper goes much further. The budgeted plans for DUNE provide a large active volume, a huge overburden, and excellent technical capabilities, including at MeV energies (for supernova neutrinos) [25–27]. For a solar-neutrino program, DUNE will need to improve data acquisition capabilities, better reject MeV backgrounds, and stimulate measurements of MeV neutrino-argon cross sections. The required investments would enhance DUNE’s planned programs. Further technical studies will be needed to fully assess our proposal.

In the following, we review the challenges in solar neutrinos, outline our proposed strategy for DUNE, calculate the signals and backgrounds, calculate the physics reach, define technical requirements, and conclude. In Supplemental Material (S.M.), we provide further details. Throughout, we make conservative assumptions.

Solar neutrinos: status and obstacles.— The fundamental challenge in solar neutrinos is disentangling neutrino-mixing effects and source properties. Super-Kamiokande (Super-K) and Sudbury Neutrino Observatory (SNO) measurements of ^8B neutrinos dominate the precision of solar determinations of $\sin^2 \theta_{12}$ and Δm_{21}^2 , as well as $\phi(^8\text{B})$, the total ^8B flux (assuming no mixing with sterile neutrinos) [5, 6, 15, 32]. The *hep* flux, $\phi(\text{hep}) \sim 10^{-3} \phi(^8\text{B})$, has not been detected [33, 34].

Their measurements of the spectra induced by neutrino interactions above a few MeV are consistent with an energy independent ν_e survival probability, $P_{ee} \simeq \sin^2 \theta_{12}$; the lack of an observed upturn in P_{ee} at low energies sets an upper limit on Δm_{21}^2 [5, 6]. Within the theoretical framework of matter-affected neutrino mixing [35–40], these results are consistent with lower-energy solar neutrino data [1–4]. Two other contributions were key to further progress:

- SNO separately measured $\phi(^8\text{B})$ and $\sin^2 \theta_{12}$ by combining data on two channels: $\nu_{e,\mu,\tau} + d \rightarrow \nu_{e,\mu,\tau} + p + n$, which is equally sensitive to all active flavors, and hence measures the total flux, and $\nu_e + d \rightarrow e^- + p + p$, from which they can then extract the mixing angle. Further progress on $\sin^2 \theta_{12}$ is limited by the 4% precision of $\phi(^8\text{B})$ from the now-completed SNO [5].

- Using the $\nu_{e,\mu,\tau} + e^- \rightarrow \nu_{e,\mu,\tau} + e^-$ channel, Super-K

isolated Δm_{21}^2 by measuring the day-night flux asymmetry (at 3σ) [6], where the ν_e survival probability at night is increased by several percent due to the matter effect in Earth [40–43]. Progress is limited by the slow increase of statistics after 20 years of exposure.

Unique advantages of DUNE.— DUNE will be located in the Homestake mine in South Dakota, at a depth of 4300 m.w.e., and will consist of homogeneous volumes of liquid argon (LAr). Each of two modules (eventually four) will have a fiducial mass of 10 kton and a larger active mass, with ~ 1 m of LAr shielding. Readout is by the time-projection technique — drifting charge deposited in the volume onto wire planes at the boundaries — plus prompt detection of scintillation light [25–27, 44].

DUNE can simultaneously measure neutrino-mixing parameters and solar-neutrino fluxes. Here we state our underlying ideas and give simple estimates; our main results are based on full calculations.

- The degeneracy between $\sin^2 \theta_{12}$ and $\phi(^8\text{B})$ can be broken by measuring two detection channels:

$$\nu_e + {}^{40}\text{Ar} \rightarrow e^- + {}^{40}\text{K}^*, \quad (1)$$

for which the rate scales as $R_{\text{Ar}} \propto \phi(^8\text{B}) \times \sin^2 \theta_{12}$, and

$$\nu_{e,\mu,\tau} + e^- \rightarrow \nu_{e,\mu,\tau} + e^-, \quad (2)$$

which scales as $R_e \propto \phi(^8\text{B}) \times (\sin^2 \theta_{12} + \frac{1}{6} \cos^2 \theta_{12})$. These channels can be adequately separated with a crude angular cut. Though the dependence on the $\nu_{\mu,\tau}$ content is weak, DUNE can improve on SNO due to its huge statistics. Figure 3 illustrates this.

- Δm_{21}^2 can be isolated through the day-night flux asymmetry, $A_{D/N} = (D - N)/\frac{1}{2}(D + N)$, which scales as $\propto E_\nu/\Delta m_{21}^2$. For the solar Δm_{21}^2 , an exposure of 100 kton-year, and using only events above 6 MeV and outside the forward cone, we expect $D = 3.04 \times 10^4$ and $N = 3.29 \times 10^4$ signal events, along with 0.83×10^4 background events in total. Considering only statistical uncertainties, $A_{D/N} \simeq -(7.9 \pm 0.8)\%$ ($\sim 10\sigma$). Though Super-K has a head start, DUNE can improve on it because the $\nu_e + {}^{40}\text{Ar}$ channel has a larger cross section, emphasizes larger neutrino energies, and a tighter relation between neutrino and electron energy.

Solar neutrinos in DUNE.— The MeV-range capabilities of DUNE [25–27] are designed to detect supernova neutrino bursts. Above 5 MeV, electrons are expected to be detected with high efficiency and 7% energy-independent energy resolution [27]. For solar signals, electrons lose energy dominantly by ionization, as the critical energy of LAr is 32 MeV [45–47]. The angular resolution of DUNE is uncertain, so we adopt simulation results for ICARUS [29], with a smearing of $\sim 25^\circ$. We present signal and background spectra calculated with conservative assumptions. Below, we discuss how the spectra could change with different assumptions.

We use neutrino spectra from Refs. [48, 49] and radial distributions from the BS05(OP) model of Refs. [21, 22]. As nominal fluxes, we use $\phi(^8\text{B}) = 5.25 \times 10^6 \text{ cm}^{-2} \text{ s}^{-1}$

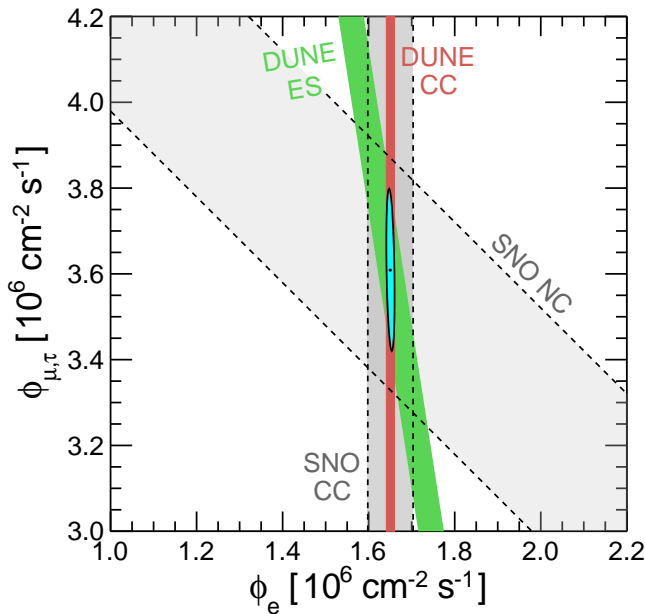


FIG. 3. Estimated precision of the ν_e and $\nu_{\mu,\tau}$ content of the ${}^8\text{B}$ flux, present (SNO [5, 67]) and future (DUNE), with the ellipse for DUNE alone. Based on a simplified analysis, with only statistical uncertainties (1σ) but assuming 2 d.o.f., and with SNO fluxes slightly rescaled to match their global-fit ${}^8\text{B}$ flux. Note the small axis ranges. Full analysis given in text.

(4% uncertainty; from SNO [5]) and $\phi(\text{hep}) = 8.25 \times 10^3 \text{ cm}^{-2} \text{ s}^{-1}$ (30% uncertainty; from theory [24, 50]). The endpoint energies are $\simeq 15$ and $\simeq 19$ MeV.

For the charged-current (CC) channel $\nu_e + {}^{40}\text{Ar}$ [51–65], the nominal threshold is $Q_{\text{gs}} = 1.5$ MeV [66], corresponding to the ground state of ${}^{40}\text{K}$, but this transition is forbidden. Instead, the cross section is dominated by transitions to nuclear excited states in ${}^{40}\text{K}^*$ (a super-allowed Fermi transition with $\Delta E_i = 4.4$ MeV, plus several Gamow-Teller transitions), which promptly produce gamma rays by nuclear de-excitation. Due to these nuclear thresholds, DUNE is most sensitive to $E_\nu \gtrsim 9$ MeV. We define the detectable energy of an event as the electron kinetic energy T_e , given by $T_e = E_\nu - Q$, where $Q = Q_{\text{gs}} + \Delta E_i$, conservatively neglecting the detectability of the ΔE_i in gamma rays. The electrons are emitted near-isotropically. Further details, including cross section uncertainties, are discussed below and in S.M.

For the elastic-scattering (ES) channel $\nu_{e,\mu,\tau} + e^-$, there is no threshold and the cross section is known with sub-percent precision [68]. All flavors participate, but the sensitivity to the $\nu_{\mu,\tau}$ content is reduced, as these have only neutral-current couplings. For this channel, DUNE is sensitive to $E_\nu \gtrsim 5$ MeV, though the broad differential cross section effectively raises that. The direction of the scattered electron is well correlated to the neutrino direction, with a maximum scattering angle of about 20° for $T_e = 5$ MeV, made worse by angular smearing. We

adequately separate $\nu_{e,\mu,\tau} + e^-$ and $\nu_e + {}^{40}\text{Ar}$ events by defining a forward cone of half-angle 40° , maximizing the signal to background ratios for both event categories in the cone away from the Sun and its complement. Inside the cone, which includes 81% of $\nu_{e,\mu,\tau} + e^-$ events [29], they dominate; outside the cone, which includes 88% of $\nu_e + {}^{40}\text{Ar}$ events, they dominate.

In principle, DUNE could use the neutral-current (NC) channel $\nu_{e,\mu,\tau} + {}^{40}\text{Ar} \rightarrow \nu_{e,\mu,\tau} + {}^{40}\text{Ar}^*$, where the final state is detected through nuclear gamma rays [59, 61, 69]. We treat this as a background because the cross section seems small. If it turns out to be larger, this channel could be important.

Backgrounds must be mitigated with standard MeV-detector techniques: defining a fiducial volume, removing U/Th from liquids and Rn from air, selecting low-background materials, applying a short deadtime after high-energy events, and so on [1–8, 70, 71]. Three important backgrounds will remain. First, neutron captures on ${}^{40}\text{Ar}$, which release a total of 6.1 MeV in several gamma rays [72–74]; these gammas Compton scatter or pair produce electrons. These neutrons, most less than a few MeV, are dominantly produced by (α, n) interactions in the rock following U/Th-chain decays [29, 75, 76]. Once they enter the detector, they can capture anywhere in the volume, due to their small cross section on argon. We assume a hermetic, passive water (/oil/plastic) shield of thickness 40 cm, which reduces this background by $\sim 4 \times 10^3$. Below, we discuss how this program can be done without shielding. Second, neutral-current $\nu_{e,\mu,\tau} + {}^{40}\text{Ar}$ events cause a peak near 9 MeV [69]. Third, emerging at the highest energies, beta-decaying radioactivities induced by muons and their secondaries [77–80], for which we apply simple cuts. Details in S.M.

Figure 4 shows the solar-neutrino signal and background spectra in DUNE as a function of detected energy. Our calculations include three-flavor neutrino mixing effects [35–42], realistic detection effects (differential cross sections [60, 81–83], energy smearing, angular cuts [29], background reduction [66, 84–97]), and a 100 kton-year exposure.

For ${}^8\text{B}$ events, the two channels are well separated and have superb yields. For $\nu_e + {}^{40}\text{Ar}$, there are 9.9×10^4 events above 5 MeV and outside the forward cone. For $\nu_{e,\mu,\tau} + e^-$, there are 2.6×10^4 events inside the forward cone. This channel provides better sensitivity to lower-energy neutrinos and the only sensitivity to $\nu_{\mu,\tau}$. For *hep* events, the $\nu_e + {}^{40}\text{Ar}$ channel allows clear separation at high electron energies, with 150 events above 11 MeV (the $\nu_{e,\mu,\tau} + e^-$ channel, which we include, is not shown).

DUNE physics reach.— DUNE can significantly improve the precision of solar-neutrino observables. We quantify this by jointly fitting (without priors) four parameters: $\sin^2 \theta_{12}$, Δm_{21}^2 , $\phi({}^8\text{B})$, $\phi(\text{hep})$. When reporting projected uncertainties for n parameters, we marginalize over the others, adopting $\Delta\chi^2$ confidence levels for n d.o.f. We assume that new physics affecting solar neutrinos is reflected in mixing-parameter values that dif-

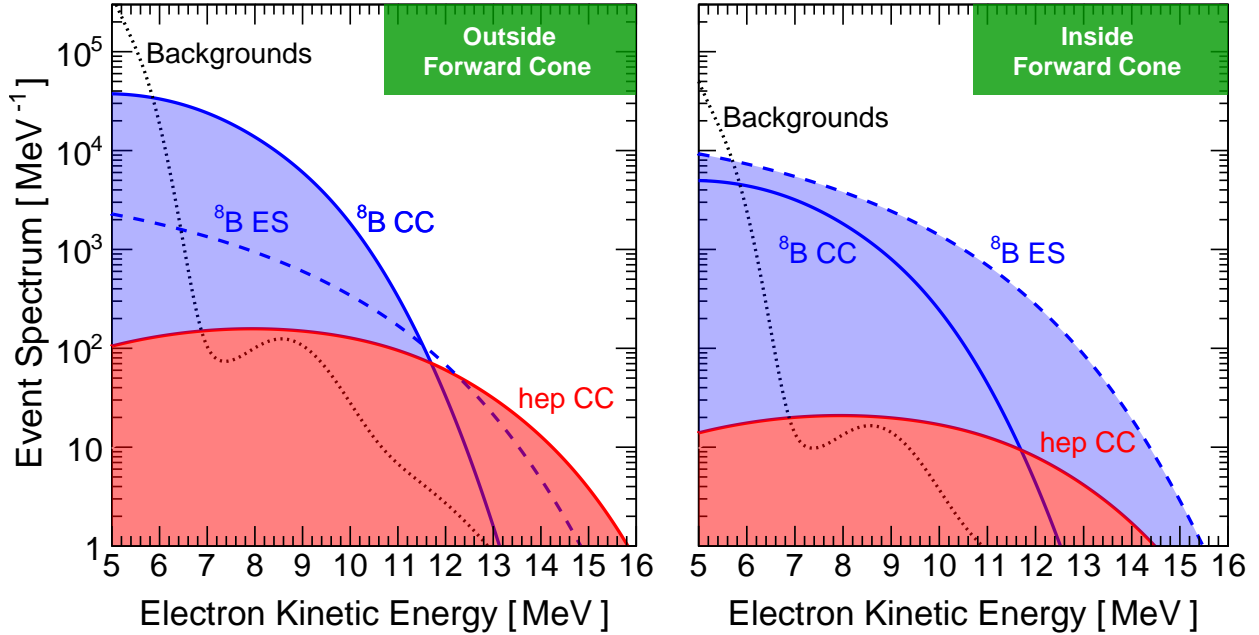


FIG. 4. Predicted solar-neutrino signals and backgrounds in DUNE for 100 kton-year, using a forward cone of half-angle 40° and (here only) combining day and night data. We include all factors discussed in the text (neutrino mixing, neutrino interactions, background reductions, energy resolution, and so on).

fer from the reactor values; to test the sensitivity to particular models, dedicated studies are needed. For a simulated dataset, we use the theoretically expected counts for signals and backgrounds, with Poisson statistics. We do not consider systematics uncertainties; further work is needed. Some will cancel in the ratio of reaction channels and the ratio of day and night spectra.

We partition data into bins of energy, bins of Earth zenith angle (night only), and outside/inside the forward cone (as in Fig. 4). We use the total electron spectra, assuming only statistical separation of the components, and not requiring reconstruction of the neutrino energy.

Figure 2 shows the projected precision for DUNE's measurement of neutrino mixing parameters, assuming the solar best-fit values ($\sin^2 \theta_{12} = 0.308$, $\Delta m_{21}^2 = 4.85 \times 10^{-5} \text{ eV}^2$ [6]). The uncertainties are 3.0% and 5.9%, respectively, each a factor $\simeq 3$ better than from all solar experiments to date, as shown in Fig. 1. The sensitivity to Δm_{21}^2 comes primarily from the day-night effect (10.4σ). The ^8B flux (marginalizing over other parameters) can be measured to 2.5%, a factor $\simeq 1.6$ better than from SNO. DUNE can make a robust first detection of *hep* neutrinos, with a precision of 11%, a factor $\simeq 3$ better than the current theoretical uncertainty.

Going forward.— New investments are needed to enhance the MeV capabilities of DUNE. At the trigger level, this includes enhancing data acquisition, storage, and processing for a steady rate of MeV events. Calibration at MeV energies across the large detector volume

will be crucial to controlling systematics. An enhanced light-detection system would enhance MeV detection.

Backgrounds must be controlled, and the biggest concern is due to neutron captures. (We assume the application of standard background-reduction techniques.) We see three possible strategies.

1. Adding 40 cm of shielding outside the detector to reduce the neutron rate, as assumed above. This allows a low threshold ($\simeq 5.8 \text{ MeV}$) to test for shape distortions in the spectrum and to enhance particle-identification techniques. This could be enhanced by adding somewhat more shielding than discussed here, which might be considered for the second two modules of DUNE, to allow improvements beyond increased statistics.

2. Additional runtime. With less or no shielding, the effective analysis threshold would be higher. However, this can be compensated by a larger exposure than 100 kton-year. With 30, 20, 10, or 0 cm of shielding, the effective analysis threshold is $\simeq 6.2, 6.5, 6.9$, or 7.2 MeV , and the exposure needed for comparable results increases at most of a factor of ~ 2 .

3. Better particle-identification techniques. We assume neutrino-interaction events and neutron-capture events with the same electron energy are indistinguishable. This is likely too conservative because $\nu_{e,\mu,\tau} + e^-$, $\nu_e + ^{40}\text{Ar}$, and neutron capture events would have one electron, an electron with gammas, and multiple gammas, respectively. For gamma rays, the radiation length is 14 cm and Compton-scattering dominates [45], so these

event classes should be distinct.

In addition, the uncertainty on the MeV-range $\nu_e + \text{Ar}$ cross section, presently $\sim 10\%$, must be reduced to $\lesssim 1\%$. Without this, DUNE alone could not break the degeneracy between $\sin^2 \theta_{12}$ and $\phi(^8\text{B})$, though its measurements of Δm_{21}^2 and $\phi(\text{hep})$ would be unaffected. The precision of $\sin^2 \theta_{12}$ and $\phi(^8\text{B})$ could still be improved by combining DUNE with other experiments.

Concluding perspectives.— This is the first study to detail how DUNE, with a new, challenging but realistic solar-neutrino program, would open substantial discovery space in both particle physics and astrophysics. A key aspect of our work is the extensive consideration of the primary obstacles and how to surmount them. With DUNE’s precision measurements of $\sin^2 \theta_{12}$ and Δm_{21}^2 , the comparison to JUNO’s may reveal new particle physics of neutrinos. Simultaneously, with DUNE’s precision measurements of $\phi(^8\text{B})$ and $\phi(\text{hep})$, it may reveal new astrophysics by testing the solar core temperature, helping to solve the solar metallicity puzzle, and probing the highest-energy fusion process. Further technical studies are needed to evaluate our proposal and to optimize its sensitivity.

No other planned experiment has been shown potentially capable of meeting all of these goals. Of proposed experiments, Hyper-Kamiokande (Hyper-K) [98, 99] stands out for its capabilities and prospects. We see a strong case that these solar-neutrino measurements, due to their importance and difficulty, require both DUNE and Hyper-K, which have complementary strengths. While DUNE would probe $\sin^2 \theta_{12}$ and $\phi(^8\text{B})$ by using two detection channels, $\nu_e + ^{40}\text{Ar}$ and $\nu_{e,\mu,\tau} + e^-$, Hyper-K would have only one, $\nu_{e,\mu,\tau} + e^-$, but the statistics would be huge. DUNE and Hyper-K would measure Δm_{21}^2 (from the day-night asymmetry) comparably well. Hyper-K would have a significant advantage on measuring the upturn in the ν_e survival probability. DUNE would measure $\phi(\text{hep})$ much better. The combined im-

pact of DUNE and Hyper-K would be significantly enhanced by new experiments for low-energy solar neutrinos [30, 100, 101].

Solar neutrino studies, begun long ago, are not done. DUNE can lead the next generation of discoveries.

Acknowledgments

For helpful discussions, we are grateful to Manojee Bhattacharya, Ed Blucher, Steve Brice, Mauricio Bustamante, Gustavo Cancelo, David Caratelli, Flavio Cavanna, Alex Friedland, Dick Furnstahl, Cristiano Galbiati, Alejandro Garcia, Mathew Graham, Jeff Hartnell, Alex Himmel, Brennan Jordan, Josh Klein, Eligio Lisi, Joe Lykken, Kenny Ng, Gabriel Orebi Gann, Ornella Palamara, Wendy Panero, Stephen Parke, Ryan Patterson, David Schmitz, Kate Scholberg, Michael Smy, Mark Vagins, Francesco Vissani, Petr Vogel, and Kyle Wendt.

The work of all authors was supported by NSF Grants PHY-1404311 and PHY-1714479 awarded to JFB. FC was later supported by Deutsche Forschungsgemeinschaft Grants EXC 153 and SFB 1258, as well as by European Union Grant H2020-MSCA-ITN-2015/674896. SWL was also supported by an Ohio State Presidential Fellowship, and later at SLAC by the Department of Energy under contract number DE-AC02-76SF00515.

Author Information

capozzi@mpp.mpg.de, 0000-0001-6135-1531
 shirleyl@slac.stanford.edu, 0000-0002-2157-8982
 zhu.1475@osu.edu, 0000-0003-0031-634X
 beacom.7@osu.edu, 0000-0002-0005-2631

We speak for ourselves as theorists, not on behalf of the DUNE Collaboration. This work is based on our ideas, our calculations, and publicly available information.

-
- [1] B. T. Cleveland, T. Daily, R. Davis, Jr., J. R. Distel, K. Lande, C. K. Lee, P. S. Wildenhain, and J. Ullman, *Astrophys. J.* **496**, 505 (1998).
- [2] M. Altmann *et al.* (GNO), *Phys. Lett. B* **616**, 174 (2005), arXiv:hep-ex/0504037 [hep-ex].
- [3] J. N. Abdurashitov *et al.* (SAGE), *Phys. Rev. C* **80**, 015807 (2009), arXiv:0901.2200 [nucl-ex].
- [4] G. Bellini *et al.* (Borexino), *Phys. Rev. Lett.* **107**, 141302 (2011), arXiv:1104.1816 [hep-ex].
- [5] B. Aharmim *et al.* (SNO), *Phys. Rev. C* **88**, 025501 (2013), arXiv:1109.0763 [nucl-ex].
- [6] K. Abe *et al.* (Super-Kamiokande), *Phys. Rev. D* **94**, 052010 (2016), arXiv:1606.07538 [hep-ex].
- [7] A. Gando *et al.* (KamLAND), *Phys. Rev. D* **88**, 033001 (2013), arXiv:1303.4667 [hep-ex].
- [8] F. An *et al.* (JUNO), *J. Phys. G* **43**, 030401 (2016), arXiv:1507.05613 [physics.ins-det].
- [9] F. Capozzi, E. Lisi, and A. Marrone, *Phys. Rev. D* **92**, 093011 (2015), arXiv:1508.01392 [hep-ph].
- [10] G. Barenboim, L. Borissov, J. D. Lykken, and A. Y. Smirnov, *JHEP* **10**, 001 (2002), arXiv:hep-ph/0108199 [hep-ph].
- [11] A. Friedland, C. Lunardini, and C. Peña-Garay, *Phys. Lett. B* **594**, 347 (2004), arXiv:hep-ph/0402266 [hep-ph].
- [12] A. de Gouvea and C. Peña-Garay, *Phys. Rev. D* **71**, 093002 (2005), arXiv:hep-ph/0406301 [hep-ph].
- [13] M. Cirelli, M. C. González-García, and C. Peña-Garay, *Nucl. Phys. B* **719**, 219 (2005), arXiv:hep-ph/0503028 [hep-ph].
- [14] A. Palazzo, *Phys. Rev. D* **83**, 113013 (2011), arXiv:1105.1705 [hep-ph].
- [15] M. Maltoni and A. Yu. Smirnov, *Eur. Phys. J. A* **52**, 87 (2016), arXiv:1507.05287 [hep-ph].
- [16] F. Capozzi, I. M. Shoemaker, and L. Vecchi, *JCAP* **1707**, 021 (2017), arXiv:1702.08464 [hep-ph].
- [17] I. Esteban, M. C. González-García, M. Maltoni, I. Martínez-Soler, and T. Schwetz, *JHEP* **01**, 087 (2017), arXiv:1611.01514 [hep-ph].
- [18] F. Capozzi, E. Lisi, A. Marrone, and A. Palazzo, *Prog. Part. Nucl. Phys.* **102**, 48 (2018), arXiv:1804.09678 [hep-ph].
- [19] J. N. Bahcall and A. Ulmer, *Phys. Rev. D* **53**, 4202 (1996), arXiv:astro-ph/9602012 [astro-ph].
- [20] N. Grevesse and A. J. Sauval, *Space Sci. Rev.* **85**, 161 (1998).
- [21] J. N. Bahcall, A. M. Serenelli, and S. Basu, *Astrophys. J.* **621**, L85 (2005), arXiv:astro-ph/0412440 [astro-ph].
- [22] J. N. Bahcall, “Software and data for solar neutrino research,” (2005), [Online; accessed 2017-9-30].
- [23] M. Asplund, N. Grevesse, A. J. Sauval, and P. Scott, *Annu. Rev. Astron. Astrophys.* **47**, 481 (2009), arXiv:0909.0948 [astro-ph.SR].
- [24] N. Vinyoles, A. M. Serenelli, F. L. Villante, S. Basu, J. Bergström, M. C. González-García, M. Maltoni, C. Peña-Garay, and N. Song, *Astrophys. J.* **835**, 202 (2017), arXiv:1611.09867 [astro-ph.SR].
- [25] R. Acciarri *et al.* (DUNE), (2015), arXiv:1512.06148 [physics.ins-det].
- [26] J. Strait *et al.* (DUNE), (2016), arXiv:1601.05823 [physics.ins-det].
- [27] R. Acciarri *et al.* (DUNE), (2016), arXiv:1601.02984 [physics.ins-det].
- [28] J. N. Bahcall, M. Baldo-Ceolin, D. B. Cline, and C. Rubbia, *Phys. Lett. B* **178**, 324 (1986).
- [29] F. Arneodo *et al.*, *Nucl. Instrum. Meth. A* **455**, 376 (2000).
- [30] D. Franco *et al.*, *JCAP* **1608**, 017 (2016), arXiv:1510.04196 [physics.ins-det].
- [31] A. Ioannisian, A. Smirnov, and D. Wyler, *Phys. Rev. D* **96**, 036005 (2017), arXiv:1702.06097 [hep-ph].
- [32] G. L. Fogli, E. Lisi, A. Marrone, and A. Palazzo, *Prog. Part. Nucl. Phys.* **57**, 742 (2006), arXiv:hep-ph/0506083 [hep-ph].
- [33] J. Hosaka *et al.* (Super-Kamiokande), *Phys. Rev. D* **73**, 112001 (2006), arXiv:hep-ex/0508053 [hep-ex].
- [34] A. T. Mastbaum, *Constraining the Hep Solar Neutrino and Diffuse Supernova Neutrino Background Fluxes With the Sudbury Neutrino Observatory*, Ph.D. thesis, U. of Pennsylvania (2016).
- [35] L. Wolfenstein, *Phys. Rev. D* **17**, 2369 (1978).
- [36] S. P. Mikheev and A. Yu. Smirnov, *Sov. J. Nucl. Phys.* **42**, 913 (1985), [*Yad. Fiz.* 42,1441(1985)].
- [37] S. P. Mikheev and A. Yu. Smirnov, *Nuovo Cim. C* **9**, 17 (1986).
- [38] W. C. Haxton, *Phys. Rev. Lett.* **57**, 1271 (1986).
- [39] S. J. Parke, *Phys. Rev. Lett.* **57**, 1275 (1986).
- [40] C. Giunti and C. W. Kim, *Fundamentals of Neutrino Physics and Astrophysics* (Oxford University Press, 2007).
- [41] E. Lisi and D. Montanino, *Phys. Rev. D* **56**, 1792 (1997), arXiv:hep-ph/9702343 [hep-ph].
- [42] M. Maris and S. T. Petcov, *Phys. Rev. D* **56**, 7444 (1997), arXiv:hep-ph/9705392 [hep-ph].
- [43] W. C. Forsythe, E. J. J. Rykiel, R. S. Stahl, W. H., and S. R. M., *Ecological Modelling* **80**, 87 (1995).
- [44] A. Marchionni, *Ann. Rev. Nucl. Part. Sci.* **63**, 269 (2013), arXiv:1307.6918 [physics.ins-det].
- [45] C. Patrignani *et al.* (Particle Data Group), *Chin. Phys. C* **40**, 100001 (2016).
- [46] S. Amoroso *et al.* (ICARUS), *Eur. Phys. J. C* **33**, 233 (2004), arXiv:hep-ex/0311040 [hep-ex].
- [47] R. Acciarri *et al.* (MicroBooNE), *JINST* **12**, P09014 (2017), arXiv:1704.02927 [physics.ins-det].
- [48] W. T. Winter, S. J. Freedman, K. E. Rehm, and J. P. Schiffer, *Phys. Rev. C* **73**, 025503 (2006), arXiv:nucl-ex/0406019 [nucl-ex].
- [49] J. N. Bahcall, *Phys. Rev. C* **56**, 3391 (1997), arXiv:hep-ph/9710491 [hep-ph].
- [50] T. S. Park, L. E. Marcucci, R. Schiavilla, M. Viviani, A. Kievsky, S. Rosati, K. Kubodera, D. P. Min, and M. Rho, *Phys. Rev. C* **67**, 055206 (2003), arXiv:nucl-th/0208055 [nucl-th].
- [51] E. J. Konopinski, *The Theory of Beta Radioactivity* (Oxford University Press, 1950).
- [52] W. E. Ormand, P. M. Pizzochero, P. F. Bortignon, and R. A. Broglia, *Phys. Lett. B* **345**, 343 (1995), arXiv:nucl-th/9405007 [nucl-th].
- [53] M. Bhattacharya *et al.*, *Phys. Rev. C* **58**, 3677 (1998).
- [54] J. F. Beacom and P. Vogel, *Phys. Rev. D* **60**, 033007 (1999), arXiv:astro-ph/9811350 [astro-ph].
- [55] P. Vogel and J. F. Beacom, *Phys. Rev. D* **60**, 053003

- (1999), arXiv:hep-ph/9903554 [hep-ph].
- [56] J. F. Beacom and S. J. Parke, Phys. Rev. D **64**, 091302 (2001), arXiv:hep-ph/0106128 [hep-ph].
 - [57] A. Kurylov, M. J. Ramsey-Musolf, and P. Vogel, Phys. Rev. C **67**, 035502 (2003), arXiv:hep-ph/0211306 [hep-ph].
 - [58] I. Gil Botella and A. Rubbia, JCAP **0310**, 009 (2003), arXiv:hep-ph/0307244 [hep-ph].
 - [59] E. Kolbe, K. Langanke, G. Martinez-Pinedo, and P. Vogel, J. Phys. G **29**, 2569 (2003), arXiv:nucl-th/0311022 [nucl-th].
 - [60] M. Bhattacharya, C. D. Goodman, and A. Garcia, Phys. Rev. C **80**, 055501 (2009).
 - [61] M.-K. Cheoun, E. Ha, and T. Kajino, Phys. Rev. C **83**, 028801 (2011).
 - [62] T. Suzuki, M. Honma, A. B. Balantekin, T. Kajino, and S. Chiba, EPJ Web of Conferences **66**, 07025 (2014).
 - [63] J. C. Hardy and I. S. Towner, Phys. Rev. C **91**, 025501 (2015), arXiv:1411.5987 [nucl-ex].
 - [64] M. Karakoç *et al.*, Phys. Rev. C **89**, 064313 (2014).
 - [65] D. Akimov *et al.* (COHERENT), Science **357**, 1123 (2017), arXiv:1708.01294 [nucl-ex].
 - [66] National Nuclear Data Center, “NuDat 2.7,” (2016), [Online; accessed 2017-9-30].
 - [67] B. Aharmim *et al.* (SNO), Phys. Rev. C **87**, 015502 (2013), arXiv:1107.2901 [nucl-ex].
 - [68] J. N. Bahcall, M. Kamionkowski, and A. Sirlin, Phys. Rev. D **51**, 6146 (1995), arXiv:astro-ph/9502003 [astro-ph].
 - [69] R. S. Raghavan, S. Pakvasa, and B. A. Brown, Phys. Rev. Lett. **57**, 1801 (1986).
 - [70] Y. Takeuchi *et al.* (SuperKamiokande), Phys. Lett. B **452**, 418 (1999), arXiv:hep-ex/9903006 [hep-ex].
 - [71] I. Blevis *et al.*, Nucl. Instrum. Meth. A **517**, 139 (2004), arXiv:nucl-ex/0305022 [nucl-ex].
 - [72] R. Hardell and C. Beer, Physica Scripta **1**, 85 (1970).
 - [73] C. D. Nesaraja and E. A. McCutchan, Nucl. Data Sheets **133**, 1 (2016).
 - [74] National Nuclear Data Center, “CapGam,” (2013), [Online; accessed 2017-9-30].
 - [75] H. Wulandari, J. Jochum, W. Rau, and F. von Feilitzsch, Astropart. Phys. **22**, 313 (2004), arXiv:hep-ex/0312050 [hep-ex].
 - [76] L. de Viveiros, *Optimization of Signal versus Background in Liquid Xe Detectors Used for Dark Matter Direct Detection Experiments*, Ph.D. thesis, Brown U. (2010).
 - [77] S. W. Li and J. F. Beacom, Phys. Rev. C **89**, 045801 (2014), arXiv:1402.4687 [hep-ph].
 - [78] S. W. Li and J. F. Beacom, Phys. Rev. D **91**, 105005 (2015), arXiv:1503.04823 [hep-ph].
 - [79] S. W. Li and J. F. Beacom, Phys. Rev. D **92**, 105033 (2015), arXiv:1508.05389 [physics.ins-det].
 - [80] G. Zhu *et al.*, (2018), in preparation.
 - [81] H. Behrens and J. Jänecke, *Numerical Tables for Beta-Decay and Electron Capture* (Springer, 1969).
 - [82] G. K. Schenter and P. Vogel, Nuclear Science and Engineering **83**, 393 (1983).
 - [83] A. C. Hayes and P. Vogel, Ann. Rev. Nucl. Part. Sci. **66**, 219 (2016), arXiv:1605.02047 [hep-ph].
 - [84] H. Rogers, in *Metallogeny of Gold in the Black Hills, South Dakota* (Society of Economic Geologists, 1990) p. 204.
 - [85] J. K. Shultis and R. E. Faw, *Fundamentals of Nuclear Science and Engineering* (Taylor & Francis, 2002).
 - [86] A. Ferrari, P. R. Sala, A. Fasso, and J. Ranft, “FLUKA: A multi-particle transport code (Program version 2005),” (2005).
 - [87] G. Battistoni, S. Muraro, P. R. Sala, F. Cerutti, A. Ferrari, S. Roesler, A. Fasso, and J. Ranft, AIP Conf. Proc. **896**, 31 (2007).
 - [88] K. T. Lesko *et al.*, (2011), arXiv:1108.0959 [hep-ex].
 - [89] Y.-D. Chan, “The Low-Background Construction of Laboratories at the 4850-ft Level Davis Campus,” (2012).
 - [90] B. Ricci, F. Mantovani, M. Baldoncini, J. Esposito, L. Ludhova, and S. Zavatarelli, PoS **Neutel2013**, 077 (2013), arXiv:1403.4072 [hep-ex].
 - [91] J. Heise, *Proceedings, 2nd Workshop on Germanium-Based Detectors and Technologies: Vermillion, SD, USA, September 14-17, 2014*, J. Phys. Conf. Ser. **606**, 012015 (2015), arXiv:1503.01112 [physics.ins-det].
 - [92] S. Westerdale and P. D. Meyers, Nucl. Instrum. Meth. A **875**, 57 (2017), arXiv:1702.02465 [physics.ins-det].
 - [93] J. F. Beacom *et al.* (Jinping), Chin. Phys. C **41**, 023002 (2017), arXiv:1602.01733 [physics.ins-det].
 - [94] T. K. Gaisser and M. Honda, Ann. Rev. Nucl. Part. Sci. **52**, 153 (2002), arXiv:hep-ph/0203272 [hep-ph].
 - [95] K. Abe *et al.* (Super-Kamiokande), Phys. Rev. D **97**, 072001 (2018), arXiv:1710.09126 [hep-ex].
 - [96] J. F. Beacom, Ann. Rev. Nucl. Part. Sci. **60**, 439 (2010), arXiv:1004.3311 [astro-ph.HE].
 - [97] K. Bays *et al.* (Super-Kamiokande), Phys. Rev. D **85**, 052007 (2012), arXiv:1111.5031 [hep-ex].
 - [98] K. Abe *et al.* (Hyper-Kamiokande), (2011), arXiv:1109.3262 [hep-ex].
 - [99] K. Abe *et al.* (Hyper-Kamiokande), (2018), arXiv:1805.04163 [physics.ins-det].
 - [100] S. Andringa *et al.* (SNO+), Adv. High Energy Phys. **2016**, 6194250 (2016), arXiv:1508.05759 [physics.ins-det].
 - [101] J. Aalbers *et al.* (DARWIN), JCAP **1611**, 017 (2016), arXiv:1606.07001 [astro-ph.IM].

Supplemental Material

Here we provide additional details. Appendix A focuses on the $\nu_e + {}^{40}\text{Ar}$ charged-current cross section, Appendix B on our calculation of detector backgrounds for DUNE, Appendix C on our calculations of DUNE's sensitivity to solar neutrinos, and Appendix D on examples of how our results change under different assumptions.

Appendix A. SIGNAL CROSS SECTION

To exploit the full potential of a solar-neutrino program in DUNE, the total cross section for

$$\nu_e + {}^{40}\text{Ar} \rightarrow e^- + {}^{40}\text{K}^*, \quad (\text{A1})$$

when convolved with the ${}^8\text{B}$ spectrum and a detector threshold of $T_e = 5$ MeV, should be known to $\sim 1\%$. With a larger uncertainty, DUNE alone can still precisely measure Δm_{21}^2 and $\phi(\text{hep})$; DUNE in combination with other experiments can also still precisely measure $\sin^2 \theta_{12}$ and $\phi({}^8\text{B})$. See Sec. D 2.

A cross-section uncertainty of $\lesssim 2.4\%$ has been claimed based on indirect measurements, though our assessment below suggests that $\lesssim 10\%$ is more realistic. Importantly, the uncertainty is unlikely to be worse than that. Although this may be surprising, based on the larger uncertainties for neutrino-nucleus interactions at GeV energies, the physics at these low energies is much simpler. Our conclusions are robust to possible changes in the central value of the cross section. For example, a 10% change in the cross section and thus signal counts would change significances of measured parameters by $\simeq 5\%$. Only the scale of its uncertainty is important.

A precise determination of the cross section is challenging but realistic. There are ways to reduce the uncertainty on the cross section, including through a first direct measurement.

A.1 Details of Calculations

We first state the form of the cross section we use, which follows Ref. [60], which presents the most recent indirect measurements. At leading order, the total cross section is

$$\sigma(E_\nu) = \sum_i \frac{G_{F,\beta}^2 |V_{ud}|^2}{\pi} |\mathcal{M}_{o \rightarrow i}|^2 E_e^i p_e^i F(Z, E_e^i), \quad (\text{A2})$$

where i indexes transitions from the ground state of ${}^{40}\text{Ar}$ to distinct relevant nuclear excited states in ${}^{40}\text{K}$, collectively denoted with a $*$ (transitions to its ground state are forbidden by selection rules). The i -dependent terms are the amplitude squared, phase space (E_e is the electron's total energy and $p_e = v_e E_e \simeq E_e$ its momentum), and Fermi function F (to account for Coulomb effects).

i	ΔE_i [MeV]	$B_i(\text{F})$	$B_i(\text{GT})$
1	2.333		1.64
2	2.775		1.49
3	3.204		0.06
4	3.503		0.16
5	3.870		0.44
6	4.384	4.00	
7	4.421		0.86
8	4.763		0.48
9	5.162		0.59
10	5.681		0.21
11	6.118		0.48
12	6.790		0.71
13	7.468		0.06
14	7.795		0.14
15	7.952		0.97
total		4.00	8.29

TABLE I. Transition strengths for $\nu_e + {}^{40}\text{Ar} \rightarrow e^- + {}^{40}\text{K}^*$ [60]. Here we have multiplied the $B_i(\text{GT})$ values by the axial coupling constant squared (with $g_A = -1.26$), so that they have the same normalization as $B_i(\text{F})$, as appropriate for Ref. [60]. In the literature, it is not always clearly noted if $B_i(\text{GT})$ values are normalized with or without this factor. The energy of the Fermi state is taken from Ref. [53].

$G_{F,\beta}$ is the Fermi constant for beta decay (see below) and V_{ud} is the quark mixing matrix element. For each nuclear transition, which could, in principle, be identified by the total gamma-ray energy, the neutrino spectrum is sampled faithfully, weighted by cross section and shifted by the nuclear threshold.

For the final states we consider, the transition amplitudes squared can be expressed as

$$|\mathcal{M}_{o \rightarrow i}|^2 = B_i(\text{F}) + B_i(\text{GT}), \quad (\text{A3})$$

where the transitions are of the Fermi or Gamow-Teller type, or mixed [51]. For allowed Fermi transitions, which correspond to the vector part of the weak current, the leptons have total spin zero and the change in the nuclear total angular momentum is zero. For allowed Gamow-Teller transitions, which correspond to the axial-vector part of the weak current, the leptons have total spin one and the change in the nuclear total angular momentum is one or zero (but not $0 \rightarrow 0$). For $\nu_e + {}^{40}\text{Ar}$, the transitions are seemingly not mixed and the only relevant Fermi transition is super-allowed, with its strength given by a sum rule, $B(\text{F}) = N - Z = 4$ (defined for the parent nucleus) [52, 60]. For the Gamow-Teller strengths, we use those based on measurements of ${}^{40}\text{Ar}(p, n){}^{40}\text{K}^*$ in forward-angle kinematics [60]. See Table I.

Because the interaction is a 2-to-2 process and the nuclear transitions are between discrete states, the kinematics and the phase-space factor are simple. (Recoil-order corrections are $\lesssim 5$ keV, and can be neglected.)

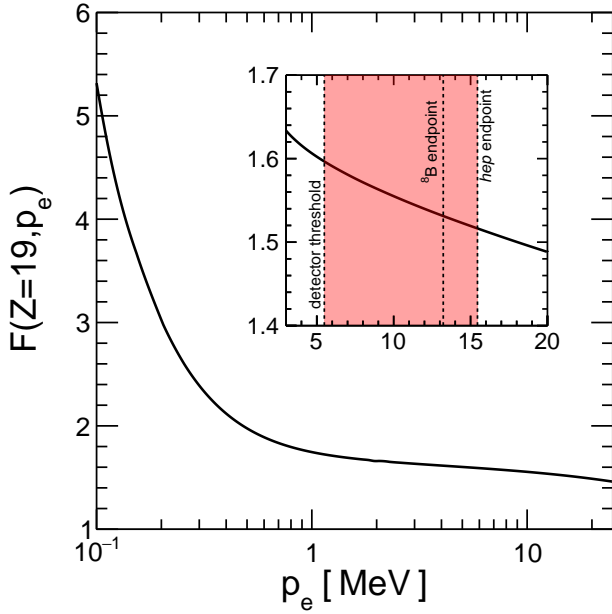


FIG. A1. Fermi function for $\nu_e + {}^{40}\text{Ar} \rightarrow e^- + {}^{40}\text{K}^*$ in terms of electron momentum, interpolated from data in Ref. [60, 81]. The shaded region indicates the approximate range of interest.

The electron kinetic energy is $T_e = E_\nu - Q_i$, where $Q_i = Q_{\text{gs}} + \Delta E_i$, with $Q_{\text{gs}} = 1.504$ MeV the reaction threshold to reach the ground state of ${}^{40}\text{K}$ (including creation of the electron) and ΔE_i the excitation energy above that [60, 66]. We assume a detection threshold of $T_e = 5$ MeV, conservatively neglecting the detectability of nuclear de-excitation gamma rays (of total energy ΔE_i), which primarily undergo Compton scattering, and may be detectable in coincidence, improving particle and reaction identification. For a neutrino interaction to register, its energy must exceed $E_\nu^{\text{thr},i} = (Q_{\text{gs}} + \Delta E_i) + 5$ MeV, which is 8.837 MeV for the lowest allowed transition and higher for others. The electron angular distribution, $d\sigma/d\cos\theta$, is $\propto 1 + \cos\theta$ for Fermi transitions and $\propto 1 - \frac{1}{3}\cos\theta$ for Gamow-Teller transitions [54, 55]. For an isotropic angular distribution, the fraction of $\nu_e + {}^{40}\text{Ar}$ events outside the forward cone is 88%. Taking into account the weighting of different transitions does not change this number appreciably.

The Fermi function F accounts for the distortion of the outgoing electron wave function due to its Coulomb interaction with the nuclear charge Z (defined for the daughter nucleus) [81–83]. For an outgoing electron, the interaction is attractive, making $F > 1$, and, in this case, the correction is substantial, a factor $\simeq 1.6$. A commonly used analytic estimate, $F \simeq 2\pi\nu/[1 - \exp(-2\pi\nu)]$, with $\nu = Z\alpha/v_e$, based on the solution to the Schrödinger equation for an electron in the potential of a point-like nucleus, is only suitable for small Z [82]. At high momentum, this is a constant; at low momentum, it varies as $1/v_e$. A detailed calculation of F , based on the solu-

tion of the Dirac equation for an electron in the potential of a finite-sized nucleus, is tabulated in Table II of Ref. [60, 81]. Figure A1 shows our interpolated result, which differs from the simple analytic expression [82] by being $\sim 10\%$ larger and by varying at large momenta, both of which are important.

Figure A2 shows the total cross section for $\nu_e + {}^{40}\text{Ar}$, combining the factors above, including the detector threshold of $T_e = 5$ MeV. At $E_\nu = 10$ MeV, a typical energy, the relevant cross section is $\sigma \approx 3 \times 10^{-42}$ cm², a factor ~ 30 larger than that for $\nu_e + e^-$, though the latter’s density of targets is 18 times higher. The $\nu_e + {}^{40}\text{Ar}$ cross section grows rapidly, faster than $\sigma \propto E_e^2 \propto (E_\nu - E_\nu^{\text{thr},i} + 5 \text{ MeV} + m_e)^2$, because with increasing neutrino energy, more nuclear thresholds are surpassed, and because of the strong effect of the detector threshold. In our calculations, we do not use this total cross section; instead, we sum the partial cross sections for each independent transition.

Figure A3 shows how different transitions contribute to the total cross section, now showing only the case where the detector threshold of $T_e = 5$ MeV is applied to each transition separately. The relative contributions vary depending on their strengths compared to those of all other kinematically accessible transitions. Below $E_\nu = 10.888$ MeV, corresponding to the threshold for the super-allowed Fermi transition, the cross section is dominated by the two lowest-energy Gamow-Teller transitions. For higher E_ν , there are four comparable contributions: each of the two lowest-energy Gamow-Teller transitions, the Fermi transition, and the sum of all other kinematically accessible Gamow-Teller transitions. (Though we do not exploit the angular distribution, doing so [54, 55] would increase sensitivity.)

In principle, there are additional contributions to the $\nu_e + {}^{40}\text{Ar}$ total cross section from particle-unbound final states, e.g., $e^- + {}^{39}\text{Ar} + p$ and $e^- + {}^{39}\text{K} + n$. However, even if the transition strengths are appreciable, the nuclear thresholds are above 9 MeV [66], making the neutrino thresholds above 14 MeV, and even higher if we account for the energy of the outgoing nucleons. For a given neutrino energy, T_e will be substantially lower than for the particle-bound transitions, burying any additional contributions in the falling total spectra of Fig. 4.

A.2 Assessment of Uncertainties

To assess the uncertainty on the cross section, we first consider two data-based evaluations. The $B_i(\text{GT})$ values we use are from the ${}^{40}\text{Ar}(p,n){}^{40}\text{K}^*$ data of Ref. [60]. For the uncertainties, we focus on the strengths themselves, though there may also be uncertainties in the excitation energies (through identification of the relevant transitions). Though the uncertainties on individual B_i are $\sim 5\text{--}20\%$, the uncertainty on the summed strength is 2.4%. This reduction in uncertainty is because the strength for the super-allowed Fermi transition is consid-

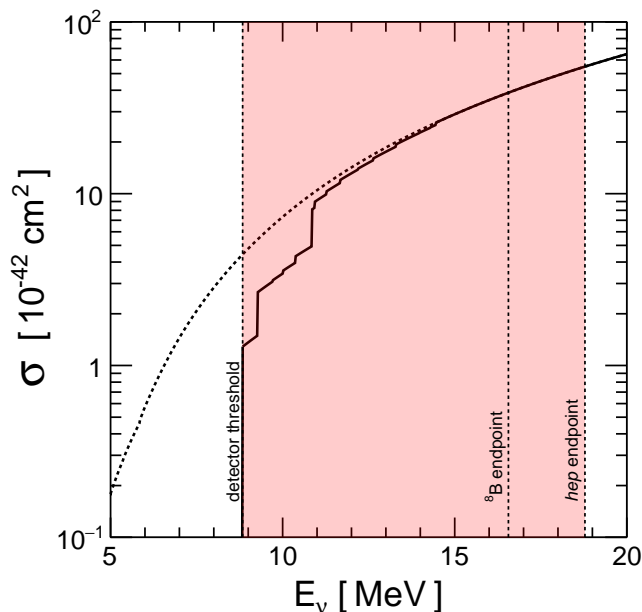


FIG. A2. Total cross section for $\nu_e + {}^{40}\text{Ar} \rightarrow e^- + {}^{40}\text{K}^*$. The solid line takes into account the 5-MeV threshold of DUNE, while the dotted line neglects it.

ered known from the sum rule and because the uncertainties of independent Gamow-Teller transitions combine in a central-limit fashion for the total strength. The uncertainty on the total cross section (convolved with the ${}^8\text{B}$ spectrum and with a detector threshold of $T_e = 5$ MeV) is comparable to that on the summed strength. In a paper preceding Ref. [60], a related group of authors obtained $B_i(F + \text{GT})$ values based on measurements of ${}^{40}\text{Ti}$ β^+ decay to ${}^{40}\text{Sc}^*$, the isospin mirror process for $\nu_e + {}^{40}\text{Ar} \rightarrow e^- + {}^{40}\text{K}^*$, with an uncertainty of 2.1% on the summed strength [53]. However, there are discrepancies between the two techniques, with the convolved cross sections at the most important energies differing at the $\sim 10\%$ level. It is difficult to assess the systematics, as the two techniques access somewhat different transitions, and both rely on some assumptions: for the (p, n) data, that the weak transitions are in the same proportions as the strong transitions; for the beta-decay data, that isospin symmetry holds. A shell-model study [64] suggests that the (p, n) data are preferred over the beta-decay data, which is one of the reasons we adopted the strengths from Ref. [60]. Further work is needed to resolve differences between the two techniques.

The cross section can also be evaluated using B_i values calculated with nuclear theory [52, 58, 59, 61, 62]. For the low energies of solar neutrinos, the preferred technique is the nuclear shell model, treating most of the nucleons as belonging to a closed core, and treating the remaining valence nucleons as subject to an effective potential from the core as well as to a residual nucleon-nucleon interaction. For the higher energies of supernova neutrinos,

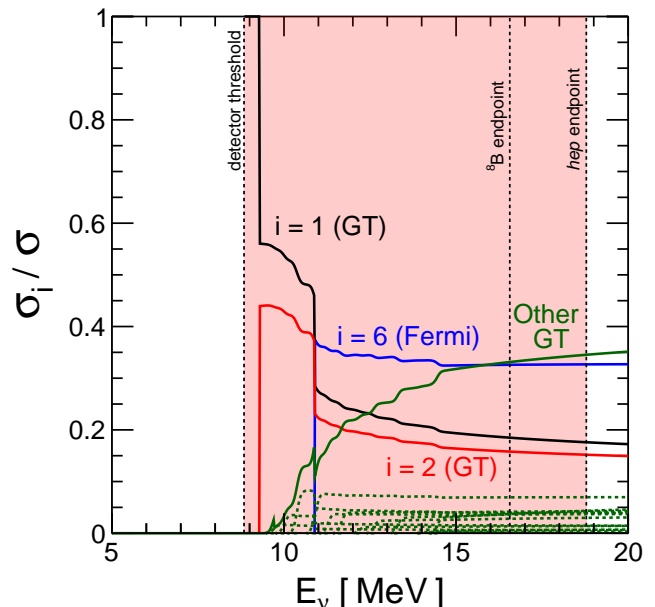


FIG. A3. Relative contributions to the total cross section for $\nu_e + {}^{40}\text{Ar} \rightarrow e^- + {}^{40}\text{K}^*$, with the minor transitions smoothed. The detector threshold is taken into account.

the preferred technique is the random phase approximation (RPA), which describes collective states of nuclei in a basis of particle-hole excitations. A hybrid approach is also possible, with RPA used to calculate transitions not well described by the shell model. Compared to our calculation, the hybrid calculation of Ref. [62], which we consider to be the most reliable, is $\simeq 10\%$ smaller. However, its B_i values for known important low-lying transitions fall well below the data of Ref. [60], allowing its cross section to be smaller, despite the additional contributions of RPA-calculated transitions ($\lesssim 10\%$ at solar-neutrino energies). We neglect the results of some other calculations: the early shell-model calculation of Ref. [52] ($\simeq 30\%$ smaller than ours, but it omits relevant nuclear operators) and the RPA calculations of Refs. [58, 59, 61] (a factor of a few difference, but they are not suited for the solar-neutrino energy range). New work is needed on all of these techniques.

Thus, based on both experimental and theoretical evaluations of the cross section, its uncertainty (for ${}^8\text{B}$ neutrinos in DUNE) is likely $\lesssim 10\%$. This is small enough that our conclusions are robust, but large enough that new efforts to reduce uncertainties are needed.

A.3 Towards Reducing Uncertainties

Even without new experimental data, it seems likely that the cross-section uncertainty can be reduced through new theoretical work: calculations of the B_i , calculations to help reconcile differences in experimental inputs,

and the development of a framework to consistently include all known effects. These effects include corrections that, while not all uncertainties per se, cause discrepancies between different results if they are not applied uniformly, of which we give several examples, following e.g., Refs. [55–57, 63, 83]. The inner radiative corrections for charged-current semi-leptonic processes with nucleons increase the cross section by $\simeq 2.4\%$, which can be absorbed into a change in the Fermi constant for beta decay ($G_{F,\beta}$) relative to that measured from muon decay (G_F). The outer radiative corrections can also increase the cross section by $\sim 1\text{--}2\%$, depending on the nucleus and how the energy deposition by bremsstrahlung affects the detectability of the electron. In principle, updating the value of the axial coupling constant from $g_A = -1.26$ to the contemporary -1.27 would also increase the cross section by $\simeq 2\%$, but g_A may be quenched in nuclei. In addition, the effects of the following should also be considered: isospin-violation corrections, subdominant argon isotopes (0.4%), particle-unbound transitions, forbidden transitions, more accurate identifications of the energies of the relevant nuclear transitions, and so on.

To reduce the uncertainty to $< 1\%$, new data are needed, starting with comprehensive new measurements of auxiliary data to evaluate B_i , e.g., from $^{40}\text{Ar}(p,n)^{40}\text{K}^*$ and ^{40}Ti β^+ decay. It seems likely that new measurements, supported by theoretical efforts, could ensure that these techniques reach their intended precision.

Ultimately, the $\nu_e + ^{40}\text{Ar}$ cross section must be directly measured with a laboratory source of neutrinos, which has never been done. Achieving an uncertainty $< 1\%$ will require the statistics of $\gtrsim 10^4$ events and commensurate control of systematics. The neutrino source could be accelerator-produced μ^+ decay at rest, for which the ν_e spectrum, before weighting with the rising cross section, peaks at $\simeq 35$ MeV. At this energy, the total charged-current cross section is $\simeq 300 \times 10^{-42} \text{ cm}^2$, taking into account only the nuclear transitions noted above; the true cross section will be larger. At the location of the suite of COHERENT neutrino detectors at the Spallation Neutron Source at Oak Ridge, the time-averaged ν_e flux is $\simeq 10^7 \text{ cm}^{-2} \text{ s}^{-1}$ [65]. We thus estimate that an exposure of ~ 10 ton-year is needed. With a low detection threshold and good collection of scintillation light, the nuclear transition of each interaction could be identified by the total energy of its de-excitation gamma rays, which would reduce backgrounds. If systematics are more challenging than statistics, then identifying specific nuclear transitions by their gamma rays could be used to measure relative strengths (including compared to the super-allowed Fermi transition) instead of the absolute cross section. There would be numerous technical challenges, but the importance of the problem encourages significant investments.

Appendix B. BACKGROUNDS

For the detection of MeV neutrinos, backgrounds must be seriously considered. Standard techniques developed for previous solar-neutrino and other experiments can powerfully reduce backgrounds. These include defining a fiducial volume, removing U/Th from liquids and Rn from air, selecting low-background materials, applying a short deadtime after high-energy events, and so on. There are some special aspects of MeV backgrounds in DUNE due to its target material, its readout technology, its unusual depth, and the fact that it is a target for GeV accelerator-produced neutrinos. We review some backgrounds that will be unimportant after standard cuts, then provide details on three that will remain important.

We first discuss the expected livetime fraction for DUNE for MeV neutrinos, i.e., when the detector is quiet from high-energy events or their aftermaths. Following a high-energy event, the produced charge takes $\simeq 2\text{--}3$ ms to drift out of the volume [25–27]. High-energy events can be created by atmospheric muons (0.05 Hz per 10 kton [27, 80]) and neutrinos from the Fermilab beam ($\simeq 1$ Hz, with duration $\simeq 10 \mu\text{s}$ [26], though the expected number of interactions per spill is tiny). In a conservative case, in which we apply a holdoff of 10 ms every 1 s, this induces a detector deadtime of only $\simeq 1\%$. As discussed below, this is enough time that any neutrons created have escaped or captured; long-lived beta-decaying isotopes must be treated separately. The expected exposure of DUNE for MeV events, i.e., when the detector is quiet, is thus nearly the same as the calendar time.

Other neutrino fluxes can be ignored. The fluxes of MeV atmospheric neutrinos [94, 95] and the Diffuse Supernova Neutrino Background [96, 97] are even smaller than that of *hep* neutrinos. The reactor flux [90, 93] is comparable to the ^8B flux, but the high threshold [66] for $\bar{\nu}_e$ events on ^{40}Ar , combined with the low energies of reactor neutrinos, make this irrelevant. For GeV atmospheric neutrinos, they can be vetoed as above.

We expect that betas and gammas from intrinsic radioactivities [29] can be mitigated effectively, leaving a negligible rate inside the fiducial volume and above 5 MeV. These long-lived radioactivities have low energies, but can effectively reach higher energies if their rate is high and/or the energy resolution is poor. Standard MeV techniques such as U/Th removal from the liquid, Rn removal from the air, and selection of low-radioactivity material can significantly lower background rates. Good energy resolution (7%) will ensure that the end-point energies of both ^{42}K (3.53 MeV, from the ^{42}Ar decay chain [66]) and ^{214}Bi (3.27 MeV, from the ^{222}Rn decay chain [66]) are too low to affect the solar analysis. We also considered backgrounds due to pileup, i.e., time and space coincidences of multiple events that could mimic a single event of higher energy. For the decays of ^{42}Ar (^{42}K) or ^{39}Ar (endpoint 0.57 MeV) [27, 29], or the capture of external neutrons (even without shielding), and requiring coincidences within $\simeq 10$ cm and $\simeq 10$ ms,

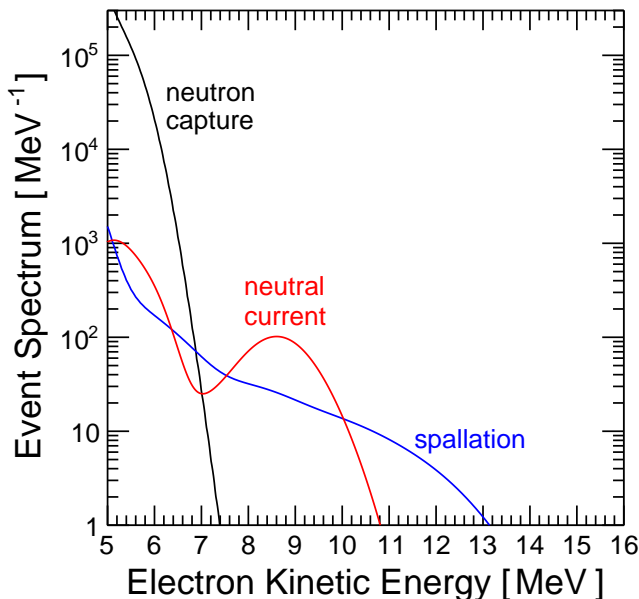


FIG. A4. Contributions of different sources of background after cuts, for an exposure of 100 kton-year, assuming 40 cm of shielding.

the rates are negligible.

Figure A4 shows the three components of the background that will remain significant after cuts. In Fig. 4, the total background yields (after cuts) outside and inside the forward cone are 14.0×10^4 and 1.9×10^4 , respectively. As in the main text, we discuss them in order of increasing energy and decreasing importance. At the end of this section, we comment on the potential impact of particle-identification techniques.

B.1 Neutron Backgrounds From Radioactivities

The dominant background is due to MeV neutrons originating in the surrounding rock. The neutrons are produced in (α, n) reactions generated by ^{238}U or ^{232}Th daughter decays as well as through the spontaneous fission of ^{238}U . Once neutrons enter the active volume, they mostly elastically scatter with argon. Within a few ms, they either exit the detector or undergo radiative capture on argon, producing multiple gamma rays with energy up to 6.1 MeV, the total energy release [72–74]. Gamma rays then Compton-scatter or pair-produce electrons with energies up to the maximum gamma-ray energy, creating signal-like events. (External gamma rays from the same processes, which we calculate, are significantly less important, due to the fiducial-volume cut.)

These neutrons cannot be rejected by the fiducial volume cut because neutrons below 5–10 MeV (above which inelastic cross sections become large) do not lose much energy through elastic scattering on argon: neutrons can

Element	weight percentage
O	46.0
Si	24.6
Fe	9.1
Al	5.4
C	3.6
Mg	2.9
Ca	2.7
K	2.7
S	1.9
Na	0.4
H	0.2
Mn	0.2
Ti	0.2
F	0.1
Th	trace (7.11 ppm)
U	trace (3.43 ppm)
total	100.0

TABLE II. The rock composition near the detector [84].

travel ~ 100 meters in LAr before they capture. (In the Sudbury Neutrino Observatory phase with pure D_2O , the neutron-capture distance was long because capture was inefficient while energy loss through elastic scattering was efficient; here, it is the opposite.) In our nominal analysis, we assume 40 cm of water or other hydrogenous shielding, which must be kept radiopure but which can be passive. Roughly, each 10 cm of water reduces the neutron background by somewhat less than an order of magnitude. Note that comparable sensitivity can be achieved with no shielding and twice the exposure.

This background rate depends on the type of rock surrounding the detector. The DUNE far detector will be placed at the 4850 feet level in the Homestake Gold Mine [26], located in Lead, South Dakota. At this level, the rock belongs mostly to the Poorman formation [26, 88, 89, 91]. The Poorman rock has an average concentration of ^{238}U of 3.43 ppm and ^{232}Th of 7.11 ppm [84], which we adopt for our calculation. This is a conservative choice, because some samples of the Poorman rock, in particular those in the Yates unit, are known to possess a sub-ppm concentration of U/Th [84], as is the case for Davis Campus where LUX is hosted [76]. Based on a survey reported in Ref. [26], we neglect the presence of rhyolite, which might increase the radioactive contamination. Regarding the concentration of other elements, we adopt the average values for the Poorman formation reported in Table 1 in Ref. [84]. This is also a conservative assumption, because the average water (OH radicals and actual water) content is $\sim 4\%$, whereas some samples show fluctuations up to 10%, which would lower the neutron level. The rock composition we adopt is reported in Table II.

We prepared dedicated simulations to assess the neutron backgrounds. For neutrons produced through (α, n) interactions, which are the most important, we use the

simulation package NeuCBOT [92] to get the neutron yield and spectrum. To calculate the neutron rate from spontaneous fission, we approximate the neutron spectrum using the Watt distribution [29, 75, 76, 85], and take the neutron yield per fission to be 2 [85]. We propagate neutrons through rock, water shielding, the active volume, and finally the fiducial volume of the detector using the simulation package FLUKA [86, 87]. We then record all neutron captures in the fiducial volume. Last, we convert the gamma ray spectrum from neutron captures [72–74] to an electron spectrum by simulating gamma rays in FLUKA. We then record the electron kinetic energy for Compton scattering and the total kinetic energy for pair production. The most important contribution to this background is neutrons of a few MeV.

There are also neutrons produced inside the detector, from (α, n) reactions generated the decay chain of ^{222}Rn that has diffused into the LAr from the rock. For a ^{222}Rn activity of $\sim 1 \text{ mBq/m}^3$ in the liquid, which has been achieved or improved upon in other detectors following air-purification procedures [70, 71], we find that this background is negligible. We neglect backgrounds that follow from the decay chains of U/Th in the detector, as LAr can be easily purified [30].

B.2 Neutrino-Argon Neutral-Current Interactions

Neutrino neutral-current interactions with argon produce an excited state of the argon nucleus:

$$\nu_{e,\mu,\tau} + {}^{40}\text{Ar} \rightarrow \nu_{e,\mu,\tau} + {}^{40}\text{Ar}^*, \quad (\text{B1})$$

where the de-excitation gamma rays might be tagged. Because there is only one shell-model calculation of neutral-current cross section [69], that is what we adopt. We calculate the cross section based on Eqs. (1, 2) and Table I in Ref. [69]. In this case, there are three excited states of argon, at 6.1, 9.6, and 10.42 MeV. The first two states emit gamma rays at the corresponding excitation energies, whereas the 10.42 MeV state leads to emission of a 6.1-MeV gamma ray.

It is difficult to access the uncertainty on the cross section. The only shell-model calculation [69] differs significantly from two RPA calculations [59, 61]. One of those [59] has a cross section that is almost a factor of 10 larger than the shell-model calculation. If that were correct, there would be a chance to turn the neutral-current channel into a signal, which would be valuable because it would detect the $\nu_{\mu,\tau}$ component of the solar flux at full strength, unlike the elastic-scattering channel. A background to the neutral-current channel would be charged-current events with the electron below threshold but the gamma-ray above. Further theoretical and experimental investigation is needed.

B.3 Cosmic-Ray Muon-Induced Backgrounds

When a cosmic-ray muon passes through the detector (for each module, the total rate is 0.05 Hz [27, 80]), it can rarely produce a large shower along its track. Secondary particles, especially pions and neutrons, may break argon nuclei and produce beta-unstable isotopes. These isotopes subsequently beta decay and produce electrons, mimicking neutrino signals. They are called spallation backgrounds (see, e.g., Refs [77–79]).

Due to the low muon rate in DUNE, spallation backgrounds can be efficiently reduced by simple cuts to reject delayed events following muons. A per-module cut of duration 250 ms, followed by a cylinder cut of radius 2.5 m and duration 40 s, induces a deadtime of only 5%. The first cut decimates short-lived radioactivities (and neutrons, which capture in a few ms), and the second greatly reduces isotopes that are longer-lived. Above 10 MeV, where spallation is most relevant, these cuts reduce the spallation background by $\simeq 99.5\%$, which is taken into account in Fig. 4. More sophisticated cuts can further reduce the backgrounds while maintaining low deadtime [80].

Muons that interact only in the nearby rock do not pose a problem. The neutrons they produce are subdominant to those produced by radioactivities in the rock. Showers induced by the muons may enter the detector, producing spallation isotopes, but these instances will be reduced by the fiducial-volume cut and our simulations show that they can be identified by the presence of charged shower particles entering the detector. Simple cuts, similar to those above, will be sufficient.

B.4 Particle-Identification Techniques

If signals and backgrounds could be separated by particle-identification techniques, that would increase the sensitivity of the solar neutrino program. As noted above, $\nu_{e,\mu,\tau} + e^-$, $\nu_e + {}^{40}\text{Ar}$, and neutron-capture events would have one electron, an electron with gammas, and multiple gammas, respectively. For gamma rays, the radiation length is 14 cm and Compton-scattering dominates [45], so these event classes should be distinct.

Once a single electron from a $\nu_e + {}^{40}\text{Ar}$ event above 5 MeV has triggered the detector, it should be possible to reconstruct, using time and space coincidences, at least some of the lower-energy electrons produced by gamma rays in association. These gamma rays carry a substantial amount of energy; see the ΔE_i values in Table I. In principle, this technique could be even employed for events in which the primary and secondary electrons are all individually below 5 MeV, but above in total. The presence of these gamma rays would strongly favor that an event is due to $\nu_e + {}^{40}\text{Ar}$. For $\nu_{e,\mu,\tau} + e^-$ events, gamma rays can be produced through bremsstrahlung, but that is suppressed because the event energies are well below the critical energy of 32 MeV [45–47]. And for neu-

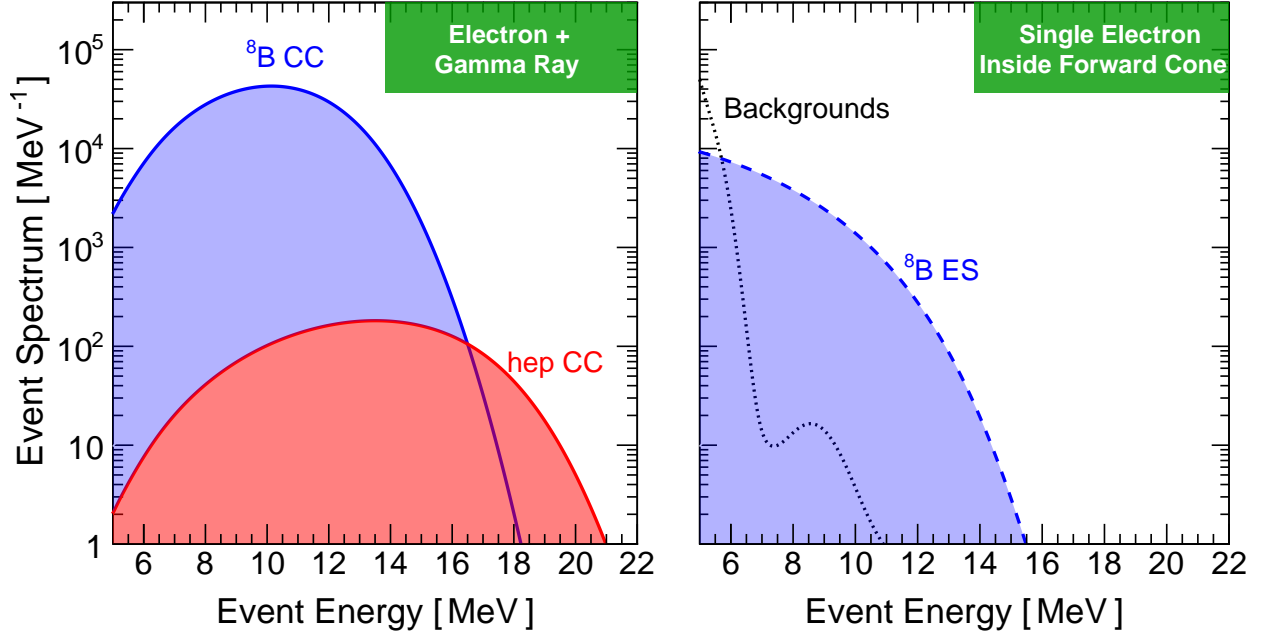


FIG. A5. Same as Fig. 4, but assuming that the full neutrino energy for $\nu_e + {}^{40}\text{Ar}$ events could be reconstructed instead of only the energy of the leading electron, which would allow separating $\nu_e + {}^{40}\text{Ar}$ events (left panel) from backgrounds and $\nu_{e,\mu,\tau} + e^-$ events (right panel).

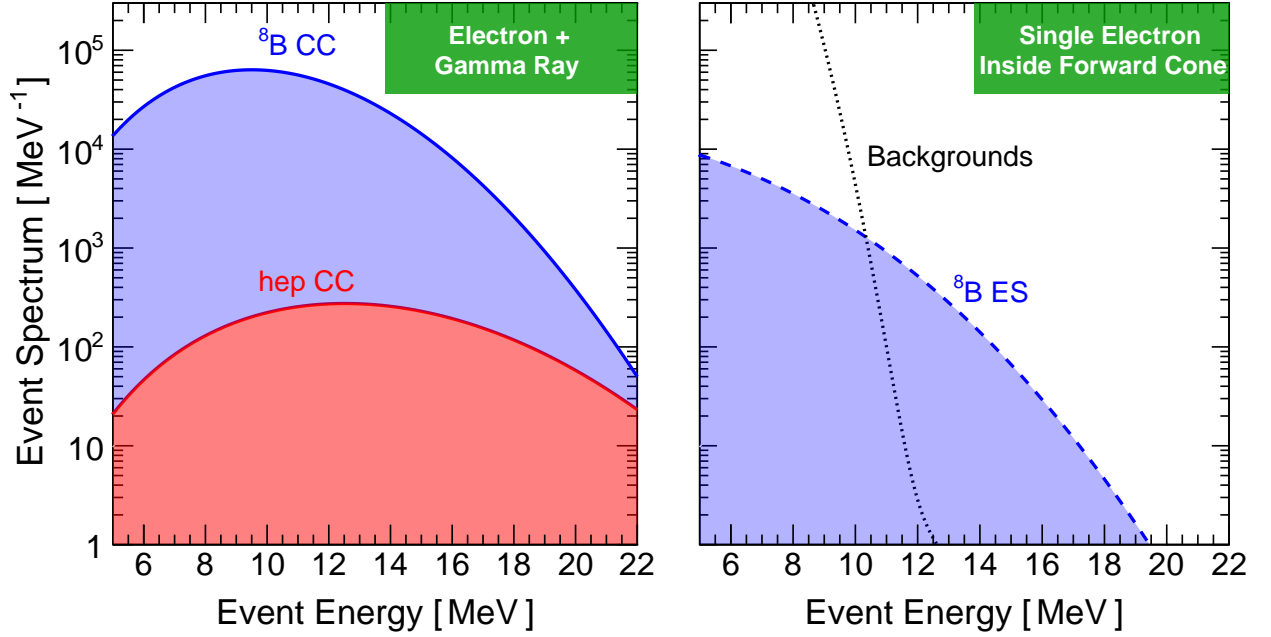


FIG. A6. Same as Fig. A5, but with no shielding and with an energy resolution of 20% instead of 7%.

tron capture, the total energy release is 6.1 MeV, with at most one gamma ray having substantial energy [72–74]. Further study is needed to assess the the potential to separate these event classes from each other (as well as from the less-important backgrounds due to $\nu_{e,\mu,\tau} + {}^{40}\text{Ar}$

events and spallation beta decays).

The impact of particle-identification techniques for $\nu_e + {}^{40}\text{Ar}$ events would be even greater if the energy deposited via gamma rays could be estimated. In our main analysis, we conservatively assumed that the only

detectable energy in an event is due to single electrons above 5 MeV. Figure A5 shows how Fig. 4 would be improved if, for $\nu_e + {}^{40}\text{Ar}$ events, the measurable energy was the full neutrino energy instead of only the leading electron energy. This would allow separation of $\nu_e + {}^{40}\text{Ar}$ events from $\nu_{e,\mu,\tau} + e^-$ events and backgrounds. Perfect separation is an unrealistic ideal, but this figure gives a sense of the benefits that would follow from being able to reconstruct at least some of the energy deposited in gamma rays. We use the full neutrino energy to account for both the measurable energy deposited by gamma rays as well for a correction of $Q_{\text{gs}} = 1.504$ MeV for the nuclear threshold; once it is known that the event is due to $\nu_e + {}^{40}\text{Ar}$, this correction is appropriate.

This capability would lead to multiple benefits. First, it would improve the precision of the measurements. Second, it would allow testing the survival probability over a wider energy range (including detecting the upturn at low energies), increasing sensitivity to new physics. Third, it would increase the robustness of the measurements to less favorable detector properties than we have assumed. For example, Fig. A6 shows how Fig. A5 would be altered by an energy resolution of 20% instead of 7% and without any shielding. In that case, the $\nu_e + {}^{40}\text{Ar}$ results would be better than we have assumed, though the $\nu_{e,\mu,\tau} + e^-$ results would be worse. The latter could be repaired by improving either energy resolution or shielding or by combining DUNE results on $\nu_e + {}^{40}\text{Ar}$ with Hyper-Kamiokande results on $\nu_{e,\mu,\tau} + e^-$.

Appendix C. ANALYSIS DETAILS

We provide technical details on our calculations of the neutrino fluxes at the detector and how the fitted parameters are deduced from the observables.

C.1 Main Analysis

As shown in the main text, we separate the events into two categories: inside and outside the forward cone, which is centered with the direction away from the Sun and has a half-angle of 40° . Each category is further divided into day and night events, each having an exposure of 50 kton-year. The day and night events are further divided into 13 energy bins, with the following extrema: 5.0, 5.5, 6.0, 6.5, 7.0, 8.0, 8.5, 9.0, 10.0, 11.0, 12.0, 13.0, 14.0, 20.0 MeV. The night events are also divided into 10 equally spaced $\cos\theta_z$ bins with a width of 0.1, where θ_z is the zenith angle of the Sun. We checked that variations in the binning do not significantly change our results.

The survival probability of ν_e for the day events is calculated using the equation

$$P_{ee}^{\text{day}}(E_\nu) = \int dr \phi_x(r) \sum_{i=1}^3 |U_{ei}|^2 |U_{ei}^\odot(E_\nu, r)|^2, \quad (\text{C1})$$

where U_{ei} and U_{ei}^\odot are the mixing matrix elements in vacuum and in matter respectively, r is the radial distance from the center of the Sun and $\phi_x(r)$ is the radial distribution of neutrinos produced in the Sun ($x = \text{hep}, {}^8\text{B}$). We take the electron density and radial distribution of ${}^8\text{B}$ and *hep* neutrinos from the solar model BS05(OP) [21, 22]. For night events we use the equation

$$P_{ee}^{\text{night}}(E_\nu, \theta_z) = \int dr \phi_x(r) \sum_{i=1}^3 |U_{ei}^\odot(E_\nu, r)|^2 P_{ie}^\oplus(E_\nu, \theta_z), \quad (\text{C2})$$

where P_{ie}^\oplus is the probability for the i -th mass eigenstate to be detected as an electron neutrino after propagating through Earth. P_{ie}^\oplus is calculated according to the method proposed in Ref. [41]. In particular, for each zenith angle bin we convolve $P_{ie}^\oplus(\theta_z)$ with the solar exposure $W(\theta_z)$ calculated for the latitude of DUNE site

$$\langle P_{ie}^\oplus(E_\nu) \rangle = \frac{\int_{\theta_{z,1}}^{\theta_{z,2}} W(\theta_z) P_{ie}^\oplus(E_\nu, \theta_z) d\theta_z}{\int_{\theta_{z,1}}^{\theta_{z,2}} W(\theta_z) d\theta_z}, \quad (\text{C3})$$

where we take the analytical expression for $W(\theta_z)$ from Ref. [41].

We generate our simulated number of data events in the i -th bin $N_i^{\text{exp}} = N_i^{\text{exp}, {}^8\text{B}} + N_i^{\text{exp}, \text{hep}}$ assuming the best fit of solar experiments, i.e. $\Delta m_{21}^2 = 4.85 \times 10^{-5} \text{ eV}^2$ and $\sin^2 \theta_{12} = 0.308$. We perform a scan of the parameter space identified by the following parameters: $\sin^2 \theta_{12}$, Δm_{21}^2 , $\phi({}^8\text{B})$, $\phi(\text{hep})$. For each point of this four-dimensional parameter space we calculate the theoretical expectation of events in the i -th bin

$$\begin{aligned} N_i^{\text{th}}(\sin^2 \theta_{12}, \Delta m_{21}^2, \alpha_{\text{sB}}, \alpha_{\text{hep}}) = \\ N_i^{\text{th}, {}^8\text{B}}(\sin^2 \theta_{12}, \Delta m_{21}^2)[1 + \alpha_{\text{sB}}] + \\ N_i^{\text{th}, \text{hep}}(\sin^2 \theta_{12}, \Delta m_{21}^2)[1 + \alpha_{\text{hep}}], \end{aligned} \quad (\text{C4})$$

where α_{sB} and α_{hep} represent the deviations from the standard values of $\phi({}^8\text{B})$ and $\phi(\text{hep})$, and we calculate the χ^2 as

$$\chi^2(\sin^2 \theta_{12}, \Delta m_{21}^2, \phi({}^8\text{B}), \phi(\text{hep})) = \sum_i^{N_{\text{bins}}} \left(\frac{N_i^{\text{exp}} - N_i^{\text{th}}(\sin^2 \theta_{12}, \Delta m_{21}^2, \alpha_{\text{sB}}, \alpha_{\text{hep}})}{\sqrt{N_i^{\text{exp}} + B_i}} \right)^2, \quad (\text{C5})$$

where B_i is the background contribution. We do not use any priors on the four parameters and we do not include energy or zenith-angle dependent systematics. The allowed regions in the space $(\sin^2 \theta_{12}, \Delta m_{21}^2)$ are obtained by marginalizing over the other parameters and by adopting the 1, 2, and 3- σ levels for 2 d.o.f., corresponding to $\Delta\chi^2 = 2.3, 6.2$, and 11.8.

C.2 Day-night Asymmetry

The significance of the day-night asymmetry is evaluated separately from the main analysis. In each of the 13

energy bins, we have the expected signal rate (charged-current events outside the forward cone only) during the day s_D^i , during the night s_N^i , and the background rate (other events outside the forward cone, including elastic-scattering) during the day and night $b_D^i = b_N^i$. Then, in each bin, we evaluate the day-night asymmetry

$$A_{D/N,i} = \frac{\phi_{D,i} - \phi_{N,i}}{\frac{1}{2}(\phi_{D,i} + \phi_{N,i})} = \frac{s_{D,i} - s_{N,i}}{\frac{1}{2}(s_{D,i} + s_{N,i} + 2b_{D,i})}. \quad (C6)$$

We calculate the total asymmetry $A_{D/N}$ through a weighted average,

$$A_{D/N} = \frac{\sum_{i=1}^{13} A_{D/N,i}/\sigma_{A,i}^2}{\sum_{i=1}^{13} 1/\sigma_{A,i}^2}, \quad (C7)$$

where the weight of each bin is its statistical uncertainty, which includes both signal and background. This gives the total uncertainty on the day-night asymmetry as

$$\sigma_A = \frac{1}{\sqrt{\sum_{i=1}^{13} 1/\sigma_{A,i}^2}}. \quad (C8)$$

For the solar best-fit parameters, this gives

$$A_{D/N} = -(7.67 \pm 0.74)\%. \quad (C9)$$

At the location of DUNE, the day and night exposures differ by a few percent [43], which would have to be taken into account in an analysis of real data (along with shut-down periods). In effect, we correct for this by assuming equal exposures, though we do use the correct location of DUNE to determine neutrino trajectories through Earth. Once corrected for, this has a negligible effect on the statistical uncertainties. Similarly for correcting for the eccentricity of Earth's orbit.

Figure A7 shows the calculated asymmetry as a function of Δm_{21}^2 . We note that $A_{D/N} \propto E_\nu/\Delta m_{21}^2$, so that the effect is enhanced at high energies, though its significance depends also on the falling statistics. Further, that symmetric uncertainties on $A_{D/N}$ lead to somewhat asymmetric uncertainties on Δm_{21}^2 .

Finally, we emphasize that the day-night sensitivity of DUNE is greater than that of Super-K [6]. Part of the reason is the increased statistics, due to the much larger cross section, but the asymmetry itself is also larger. In DUNE, higher neutrino energies are emphasized, due to the stronger energy dependence of the cross section, as well as the larger difference between neutrino and electron energy. Also in DUNE, the day-night asymmetry will be measured through a charged-current channel, avoiding dilution due to the $\nu_{\mu,\tau}$ component of the flux. Last, the tighter relation between neutrino and electron energy reduces the smearing of the day-night signal between different energy bins.

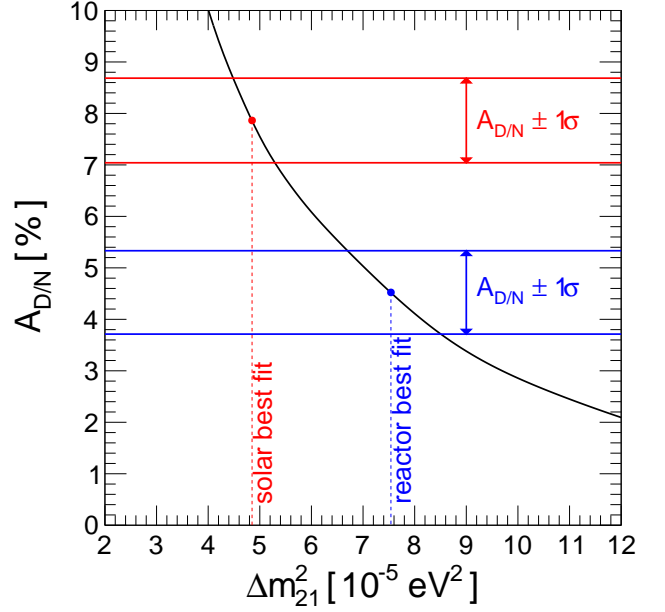


FIG. A7. The day-night asymmetry as a function of Δm_{21}^2 . The red (blue) band represents the $1\text{-}\sigma$ statistical uncertainties on $A_{D/N}$ for the solar (KamLAND) best fit.

Appendix D. EFFECTS OF INPUT CHOICES

We report how our results change with different assumptions about the inputs.

D.1 Choice of Best-Fit Mixing Parameters

In the main analysis, we generated our simulated data set assuming the best-fit value of Δm_{21}^2 from solar experiments, to study the capability of DUNE to resolving the long-standing tension with KamLAND. If we assume that there is no new effect in the propagation of solar neutrinos, the best fit of DUNE is expected to be the same as that of KamLAND. We thus also generate a simulated data set for $\Delta m_{21}^2 = 7.54 \times 10^{-5} \text{ eV}^2$.

Figure A8 shows the allowed regions at 1, 2, 3- σ in the mixing-parameter plane. The precision on $\sin^2 \theta_{12}$ is basically unchanged with respect to Fig. 2. However, now the 3- σ constraint on Δm_{21}^2 is about three times larger than what reported in Fig. 2, due to the smaller day-night asymmetry.

D.2 Assumed Detector Properties

The detection threshold, nominally 5 MeV, depends on two factors: the ability of the data-acquisition system to register, recognize, and record signals in the presence of noise, and the rate of background events in this energy range. The first seems achievable, but remains to be

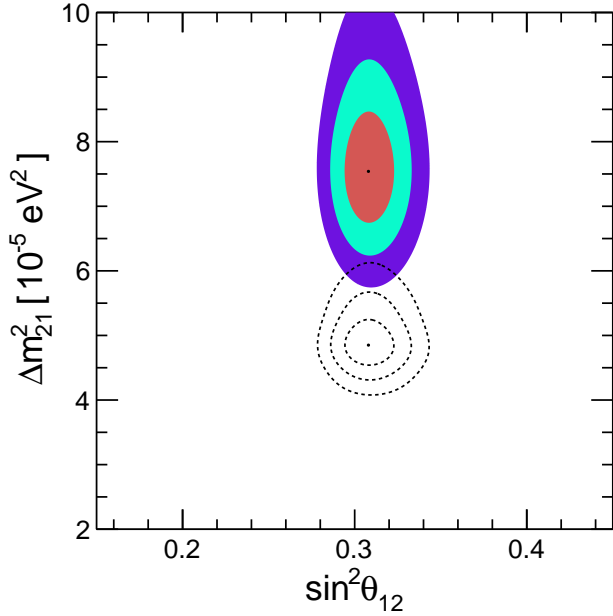


FIG. A8. Allowed regions at 1, 2, 3 σ obtained assuming $\Delta m_{21}^2 = 7.54 \times 10^{-5} \text{ eV}^2$, the global best fit value, including reactor data. The dashed contours are for the solar-only best fit value, as in Fig. 2.

demonstrated [27]. Regarding backgrounds, we show in Fig. 4 that even with shielding, neutrons are a significant background in the energy range 5–6 MeV. Figure A9 (left panel) shows that if we increase the analysis threshold to 6 MeV, the sensitivity barely changes.

To assess the impact of reduced shielding, we first consider how the mixing-parameter sensitivity depends on changes to the analysis threshold for any reason, then discuss shielding specifically. Figure A9 (right panel) shows how much the runtime must be increased to obtain mixing-parameter sensitivity comparable to that of our nominal case, with a 5-MeV threshold, 40-cm shielding, and an exposure of 100 kton-year (2.5 years of four modules, or 5 years of two modules). For increases of up to a few MeV, for which the spectra shown in Fig. 4 fall off slowly, the increases in required runtime are reasonable. Beyond that, the spectra fall steeply, and the required runtime increases quickly.

We stress that reasonable changes in the analysis threshold only affect the sensitivity through statistics, which can be restored with a longer runtime. This is because $\sin^2 \theta_{12}$ is determined from the electron-neutrino survival probability, which is near-constant at these energies, and because Δm_{21}^2 is determined from the day-night asymmetry, which increases with energy.

Reductions in the assumed shielding would increase the required analysis threshold. Because the neutron background spectrum is steep (see Fig. A4 for details), this correspondence is sharp. With 40, 30, 20, 10, or 0 cm of shielding, the effective analysis threshold is \simeq

5.8, 6.2, 6.5, 6.9, or 7.2 MeV. Even without shielding, DUNE could make world-leading measurements of solar neutrinos; to achieve comparable sensitivity to our nominal case, the required exposure would have to increase by only a factor $\simeq 2$. A low threshold is also preferred to allow tests of shape distortions in the spectrum and to enhance particle-identification techniques.

A closely related point is energy resolution, because it smears background spectra from lower to higher energies. If the energy resolution could be made better than the expected 7%, it would help the sensitivity somewhat and might help particle-identification techniques more. If the energy resolution is worse than expected, the sensitivity will be degraded. In Refs. [25–27], an energy resolution of $\simeq 20\%$ is considered if, contrary to expectations, the electron lifetime in LAr is short and corrections for this cannot be made. With this resolution and 40 cm of shielding to reduce neutron backgrounds, sensitivity compared to that of our nominal case would be obtained if the exposure were increased by only a factor $\simeq 2$. However, with this resolution and no shielding, the ability to measure solar neutrinos would largely be lost. At least one, and ideally both, of resolution and shielding, must be prioritized.

An enhanced light-detection system could help in several ways, including refining triggering; better determining the t_0 of events, important for energy resolution; and particle identification. This would also benefit supernova neutrino detection and perhaps other programs.

For angular resolution, though we assumed a smearing of 25° , following ICARUS [29], we conservatively defined the forward cone to have a half-angle of 40° . Further, we find that the results are not sensitive to reasonable variations from this.

Calibration of the full detector in the MeV range will be challenging, but is important to control systematics. On the experimental side, this will be aided by the extensive knowledge of techniques built up by earlier MeV solar and reactor neutrino experiments. Calibration sources will likely include muon decays at rest, spallation decays (where the long time between muons, ~ 20 s in each module, will allow clean samples), and neutron captures (where the high energy release, 6.1 MeV, makes the high-energy edge of the spectrum observable). These will help calibrate the energy scale, energy resolution, and absolute size of the fiducial volume. On the analysis side, control of systematics will be aided by the use of ratios (day-night, as well as the comparison of $\nu_e + {}^{40}\text{Ar}$ and $\nu_{e,\mu,\tau} + e^-$ spectra).

D.3 Impact of Cross-Section Uncertainty

In our main analysis, we neglected the uncertainty on the charged-current cross section. Here we estimate the effects of a nonzero uncertainty by assuming a normalization uncertainty of 1% or 10%. In a future work, we will consider the effects of uncertainties on individual transi-

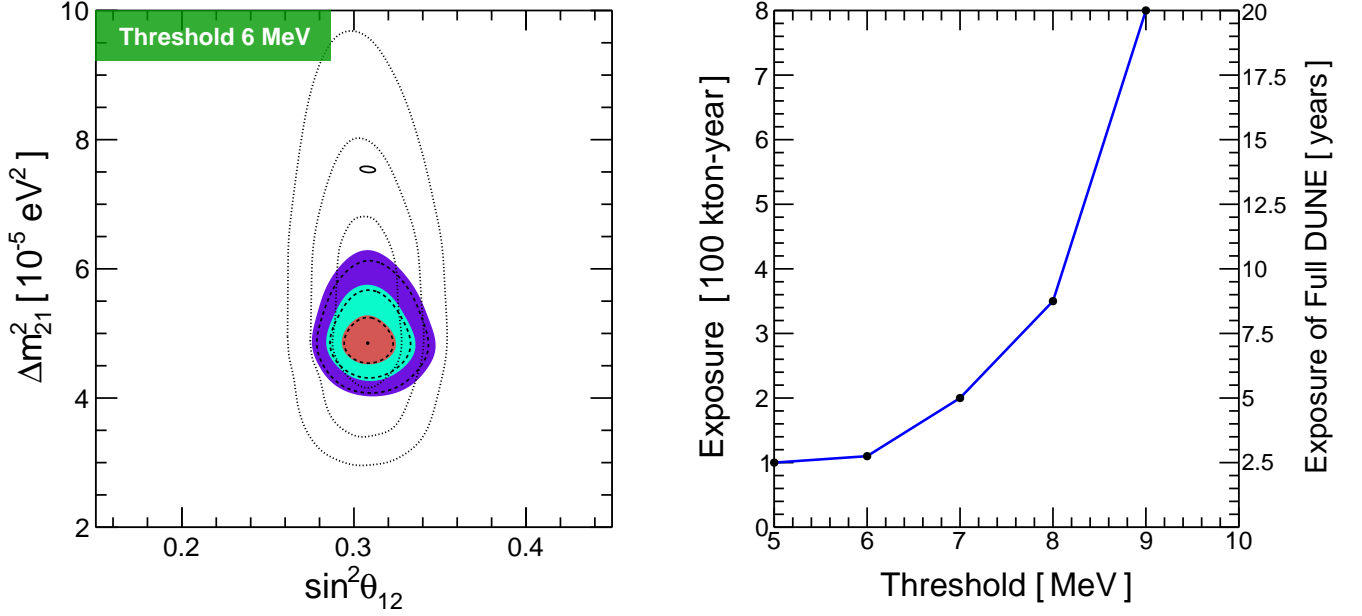


FIG. A9. **Left:** Allowed regions at 1, 2, 3- σ for a detection threshold of 6 MeV. The dashed lines are for our nominal case, with a threshold of 5 MeV (effectively $\simeq 5.8$ MeV), for which results are shown in Fig. 2. The dotted contours refer to the present sensitivity and the solid contour to the expected sensitivity of JUNO (see Figs. 1 and 2). **Right:** With varying analysis threshold, the exposure required to obtain comparable mixing-parameter sensitivity to that of our nominal case.

tion strengths. Figure A10 shows the allowed ranges of the mixing parameters in these cases. For a cross-section uncertainty of 1%, the effects are moderate, indicating that reaching this scale would be adequate. For a cross-section uncertainty of 10%, the uncertainty on $\sin^2 \theta_{12}$ is worsened significantly, while that of Δm^2_{21} is unchanged. The normalization of the charged-current event spectrum depends on the product of $\phi(^8\text{B})$, the cross section, and $\sin^2 \theta_{12}$, so they are degenerate. The elastic-scattering event spectrum depends on $\phi(^8\text{B})$, a known cross section, and a different weighting of $\sin^2 \theta_{12}$, so it can only

be used to solve for two of the three parameters. In the day-night asymmetry, all three factors cancel.

If the results of other detectors are included, then the effects of cross-section uncertainties are much less. (All results above are based on results from DUNE alone, with no priors on the parameters.) The reason is that these data help break the degeneracy in the normalization of the spectrum. Figure A11 repeats Fig. A10 but takes into account 4% Gaussian priors on $\phi(^8\text{B})$ and $\sin^2 \theta_{12}$ from solar data, and not taking advantage of their correlations. A joint fit with other data would be even more powerful.

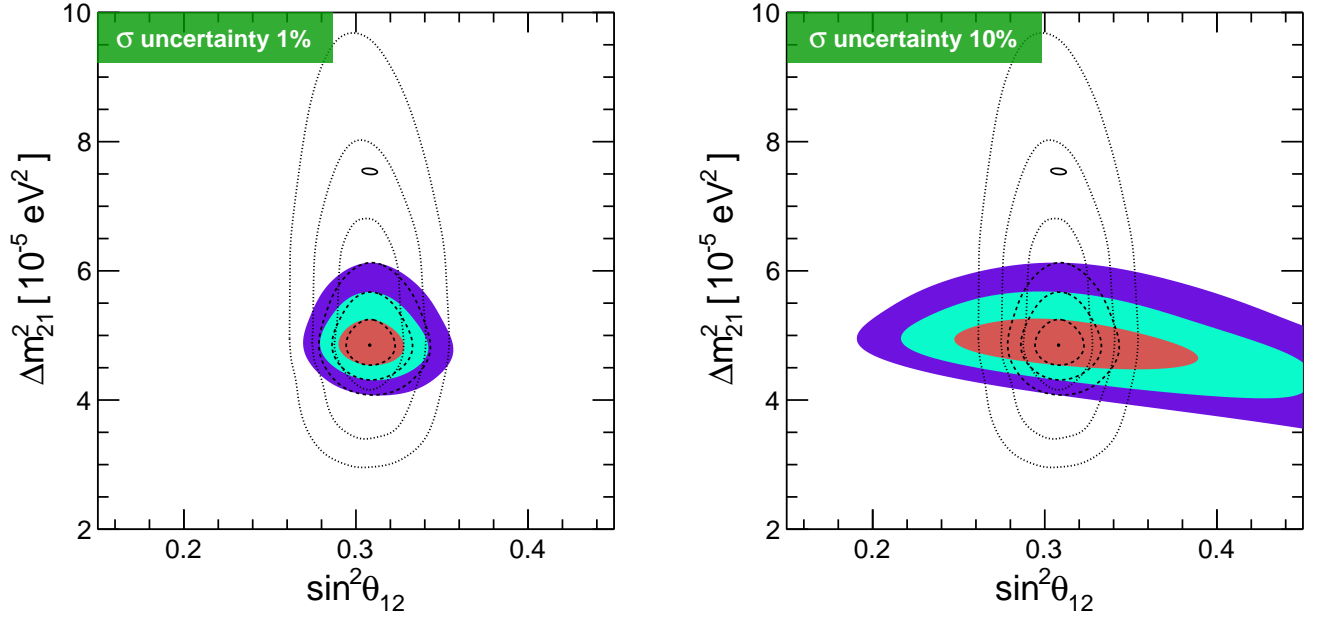


FIG. A10. Impact of the uncertainty on the charged-current cross section (1% or 10%) on the precision of the mixing parameters. The dashed lines are for our nominal case, where this uncertainty is neglected, and for which results are shown in Fig. 2.

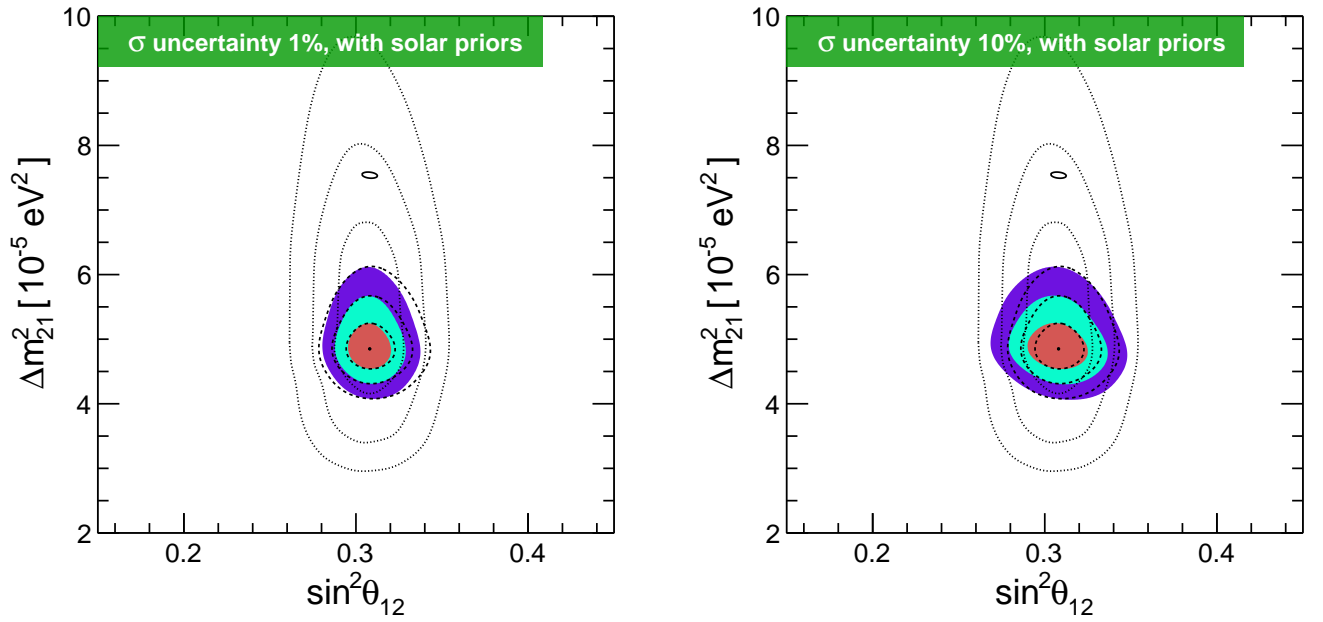


FIG. A11. The same as Fig. A10, but now including uncorrelated priors of 4% each on $\phi(^8\text{B})$ and $\sin^2 \theta_{12}$, based on solar data.